SOLID OXIDE FUEL CELL CATHODES: EXPERIMENTS ON MATERIAL STABILITY AND NOVEL TEST SYSTEM DEVELOPMENT

by

Nakkiran Arulmozhi

A thesis submitted to the Department of Chemical Engineering
In conformity with the requirements for
the degree of Master of Applied Science

Queen's University
Kingston, Ontario, Canada
(February, 2012)

Copyright ©NakkiranArulmozhi, 2012

Abstract

Cost reduction is driving the development of solid oxide fuel cell (SOFC) technology for operations at lower temperatures (500 °C -700 °C) so as to allow the usage of cheaper balance-of-plant components and enhance the durability of the stack. However, lower temperatures adversely affect the overall performance of the cell and most notably that of the cathode. Development of cathode material exhibiting high performance at lower temperature is one of the goals of SOFC research and development. This thesis work is concerned with two distinct aspects of SOFC cathode development – one concerned with the stability of a recently studied cathode material, $La_{0.5}Ba_{0.5}CoO_{3-\delta}$ (LBC), in CO_2 containing atmosphere and another concerned with the development of methods for fabrication of reproducible electrodes and rapid electrochemical testing thereof.

The study of reaction between LBC and CO_2 was carried using a combination of thermogravimetric analysis (TGA), ex-situ X-Ray Diffraction (XRD) of products from TGA experiments and in-situ high-temperature XRD of LBC-CO_2 mixtures. The mass change observed during TGA was combined with ex-situ XRD analyses of solid material phases to deduce the overall reactions. In-situ XRD measurements allowed for studying the intermediate reaction products. Isothermal studies at different temperatures in pure CO_2 yielded kinetics for the reaction between LBC and CO_2. Overall reaction pathway was proposed from these data. In addition, experiments were carried out to determine the thermodynamic carbonate formation temperature at a fixed CO_2 partial pressure (pCO_2).From the thermodynamic analysis of carbonate formation temperature at three different pCO_2, the standard state enthalpy and entropy for the carbonate formation

reaction were determined. This work is the *first* known in-depth study of reaction between LBC and CO_2.

The second distinct contribution of this thesis is the demonstration of a test system framework for fabricating reproducible miniature electrodes and rapid testing thereof. In particular, inkjet printing method was used to create well defined geometry of porous electrode and micro-contact impedance spectroscopy setup (MICS) was used to study the electrode electrochemical kinetics. The feasibility with electrode fabrication and electrochemical testing methods were demonstrated through the study of multiple silver miniature electrodes printed on single chip made of yttria-stabilized zirconia single crystal wafer.

Acknowledgements

I must thank my supervisor Dr Kunal Karan for giving me the opportunity to pursue my graduate studies in an exciting field under his guidance. His valuable inputs and suggestions shaped me both as a professional and independent individual.

I owe a huge gratitude to professors and researchers of FCRC for their continuous support throughout my graduate studies. Especially, I want to thank Dr Kenney and Dr Amin for their initial and immense contribution in developing materials and methods for our SOFC lab. I also like to thank Andrea for teaching me TGA and helping to solve technical issues. In addition, I also want to acknowledge Alan for helping me in XRD measurement.

Finally, I want to thank my parents, friends and family for their support and understanding.

Table of Contents

List of Figures

List of Tables

Chapter 1

Introduction and Background

1.1 Overview

Energy is one of the basic building blocks of nature and has a huge influence over world's economy, power and policy [1]. As the demand for energy grows every year, it has become an immense challenge to meet the energy requirements, especially in the major sectors - residential, commercial, industries and transportation [2]. Further, since the energy demands for the most part are met by fossil fuels like coal, oil and natural gas, it has an adverse impact on the environment due to greenhouse gas emissions. The energy usage and CO_2 emissions trends are shown in Figures 1(a) and 1(b), respectively.

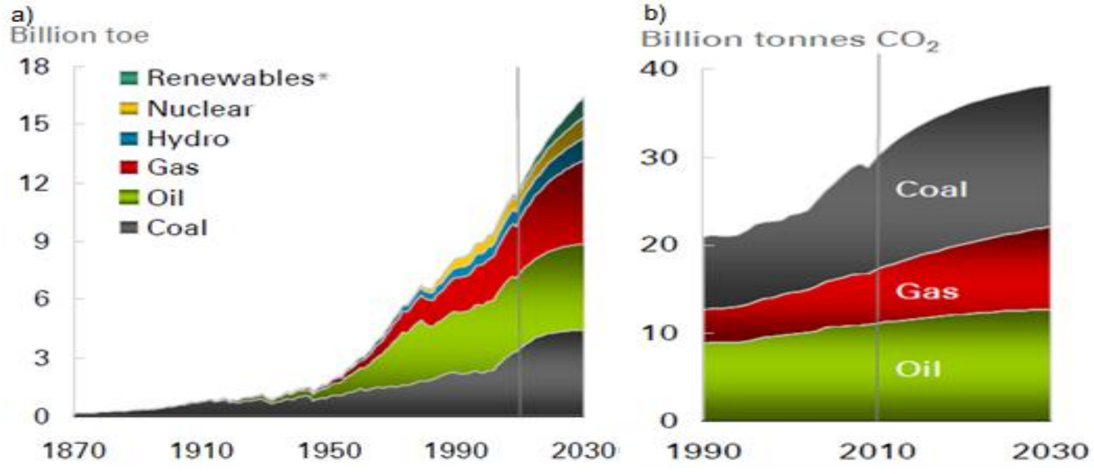

Figure 1-1 a) Trends and forecast of world energy demand by fuel and their corresponding CO_2 emission (b) (reproduced from [2])

Therefore, the current global energy scenario not only faces major challenges in the power generation but also in the mitigation of their environmental impact. This problem has accelerated a global effort in the development of green energy technologies as an alternative to the existing energy conversion technologies [3]. Fuel cells are one such energy conversion technology wherein the chemical energy of a fuel is converted to electrical energy in an efficient and environmentally friendly manner [3]. Therefore, fuel cells are expected to play an important role in the future of energy market.

Based on the material type of the electrolyte, fuel cells are classified into different classes- polymer electrolyte membrane fuel cell (PEMFC), solid oxide fuel cell (SOFC), molten carbonate fuel cell (MCFC) and alkaline fuel cell (AFC). Of these, SOFC, a solid electrolyte based fuel cell, has the advantage of high conversion efficiency and power density [4]. Most importantly, SOFC, in principle, can utilize a variety of hydrocarbon fuels because of its tolerance towards contaminants and high temperature of operation [4]. As shown in Figure 1-2, SOFCs are being designed for a variety of applications ranging from portable power (~100 W) to auxiliary power in long-haul trucks for transportation (~10 kW) to distributed (~100 kW) and centralized (>1 MW) power generation, all operating on currently available fuels.

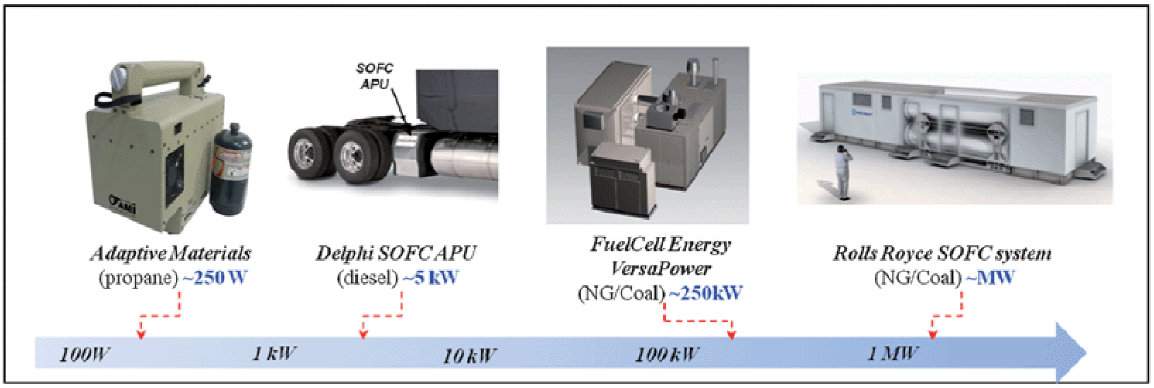

Figure 1-2 SOFC systems with wide range of power output, (reproduced from [5])

Due to its promise of fuel flexible operations and wide power output range, SOFC research programs (partnership of university, national and industrial labs) worldwide are engaged in addressing the full range of fundamental and technical problems facing the development and deployment of SOFCs.

1.2 Solid oxide fuel cell (SOFC) – General background

1.2.1 Principle of operation

A fuel cell system is designed as a combination of several stack units coupled in parallel and series to deliver desired power output [5]. Each stack unit (Figure1-3a) contains a number of single SOFC cell stacked together in-series to generate sufficiently large voltage. A single cell unit has three major components– a cathode, an electrolyte and an anode - connected to external load through interconnect.

During SOFC operation, fuel (H_2) and oxidant (O_2/air) are supplied over anode and cathode side of single cell, respectively as shown in Figure 1-3a. The single cell is the heart of a SOFC system, which comprises of five layers namely cathode current collector, cathode functional layer, electrolyte, anode functional layer and anode support (Figure 1-3b).

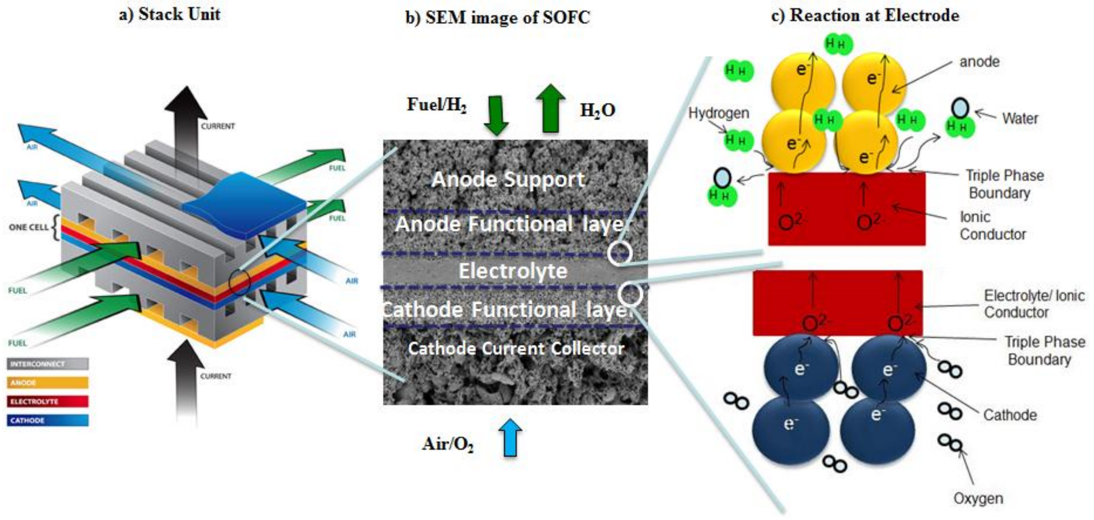

Figure 1-3 (a) Schematic diagram of a stack unit (reproduced from [24]), (b) scanning electron microscope (SEM) image of a single cell (reproduced from 26), and (c) various processes at electrode/electrolyte interface.

The oxygen supplied at the cathode side is transported through the porous layer of cathode current collector to reach the reaction site. In the cathode functional layer, oxygen reduction reaction (ORR) takes place at locations where all three phases (electrode/electrolyte/gas) are in close contact to each other (Figure 1-3c). This region is called the three-phase boundary (TPB) region. The overall cathode electrochemical reaction is

$$\frac{1}{2}O_2(gas) + \ 2e^-(cathode) \rightarrow O^{2-}(cathodeTPB) \qquad 1\text{-}1$$

Due to the chemical potential difference between the cathode and the anode, the oxide ion diffuses (via oxygen vacancies) through the solid oxide electrolyte from the cathode to the anode triple phase boundary:

$$O^{2-}(cathodeTPB) \rightarrow O^{2-}(anodeTPB) \qquad 1\text{-}2$$

On the anode side, the fuel is transported through the anode support layer to the anodic reaction site. In the anode functional layer, the fuel (H_2) is oxidized in the presence of oxide ions from the electrolyte to form H_2O (Figure 1-3c), according to the following, anode reaction:

$$O^{2-}(anodeTPB) + H_2(gas) \rightarrow H_2O + 2e^- \qquad 1\text{-}3$$

Therefore, the overall reaction for a single cell can be written as

$$\frac{1}{2}O_2 + \ H_2 \rightarrow H_2O + \ Energy \qquad 1\text{-}4$$

Under ideal conditions, the change in Gibbs free energy (ΔG) for the overall electrocatalytic reaction (eqn.1-4) would be converted totally into electrical work.

$$\Delta G(T) = \ \Delta G^{\circ}(T) + \ RTln\left(\frac{pH_2O_{anode}}{pH_{2_{anode}}\sqrt{pO_{2_{cathode}}}}\right) \qquad 1\text{-}5$$

For hydrogen (H_2) as fuel and oxygen (O_2) as oxidant gas, the ΔG for the overall reaction in the fuel cell (eqn. 1-5) is -229 kJ/mol at standard conditions (25 °C, 1 atm) [6].The

Nernst-voltage or theoretical voltage ($E_{theoretical}$) can be calculated from Gibbs free energy by applying the following equation

$$\Delta G(T) = -nFE_{theoritical} \qquad 1\text{-}6$$

where, n is the number of moles of electrons transferred in the cell reaction and *F* is the Faraday's constant, the number of coulombs per mole of electrons: $F = 9.648 \times 10^4$ C mol^{-1}. By introducing eqn.1-6 into eqn.1-5, the following expression for the hydrogen and water partial pressure dependent Nernst voltage is found to be

$$E_{theoritical} = -\frac{\Delta G^{\circ}(T)}{nF} - \frac{RT}{nF} ln\left(\frac{pH_2O_{anode}}{pH_{2_{anode}}\sqrt{pO_{2_{cathode}}}}\right) \qquad 1\text{-}7$$

In a typical SOFC operation range (600°C - 950 °C) fed with hydrogen (with 1 % H_2O) as a fuel and air as the oxidant, the values of $E_{theoretical}$ lies between 1.18 and 1.13 V. However, in an actual operating cell, a number of irreversibilities or potential losses occur. The nature and effect of irreversibilities on SOFC performance is explained in the following section.

1.2.2 SOFC electrochemical performance

As shown in the Figure 1-4a, each layer of SOFC single cell has irreversibility associated with it. These include irreversibilities arising from mass transport limitation (concentration polarization at both the anode and the cathode), ion/electron transport limitation (Ohmic loss) and electrochemical reaction overpotential (activation polarization at both the anode and the cathode).

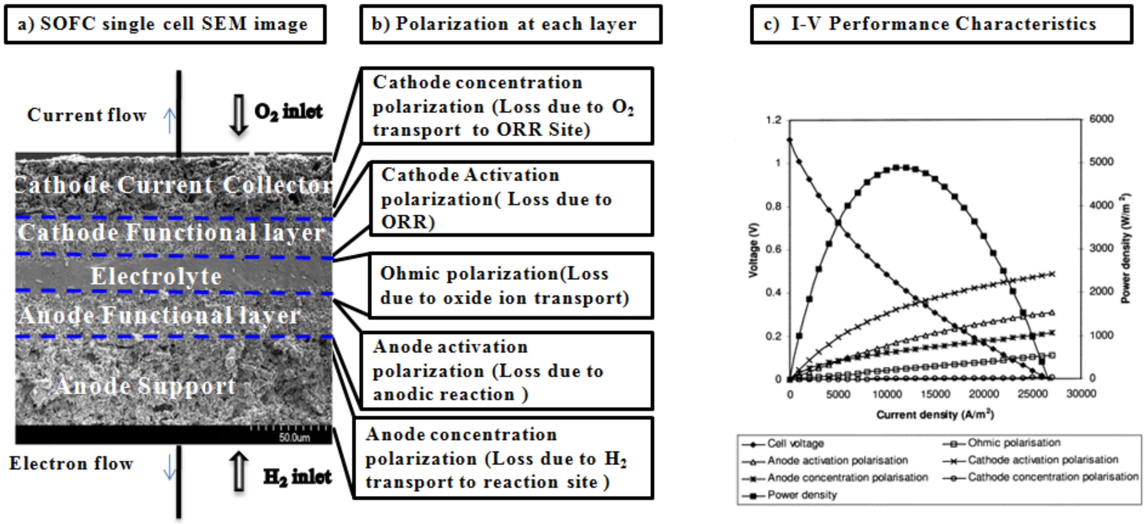

Figure 1-4 Schematic diagram of various losses at SOFC. a) Shows the SEM image of various layer of single cell, their corresponding polarization loss [reproduced from (26)](b) and I-V characteristics curve of single SOFC showing contribution of each polarization loss on fuel cell overall performance (c) [reproduced from [7]]

The effect of each of the irreversibilities on the overall cell performance is clearly shown in I-V characteristics of a SOFC single cell (Figure 1- 4c) and their inherent nature is explained below.

1.2.2.1 Activation polarization loss(η_{act})

All chemical reactions, including electrochemical reactions, involve energy barriers that must be overcome by the reacting species. In the case of fuel cells, the reaction at the electrode surface namely hydrogen oxidation and oxygen reduction has to overcome the activation energy barrier and the voltage loss associated with it is called activation polarization loss. Activation polarization loss depends mainly on intrinsic factors such as the electro-catalyst/electrolyte material, surface structure and composition of electro-catalyst in-addition to extrinsic factor such as electrode microstructure, operating temperature and pressure.

1.2.2.2 Concentration polarization loss (η_{conc})

In a porous electrode, the fuel and oxidant gases have to be transported through the gas-filled pores of the electrode to reach the reaction sites. Thus, the concentration at the reaction site can differ significantly from that in the supply stream. Since the reaction kinetics depends on the local reactant concentration, lower reactant concentration demands higher overpotential to attain same current generation. That is, mass transport effects give rise to polarization losses attributed to lower local concentration. This is called concentration polarization loss. In principle, voltage losses due to gaseous transport are function of the fundamental binary diffusivity (D), electrode microstructure, partial pressure and current density. Concentration polarization loss occurs both at the anode ($\eta_{\mathrm{conc}}^{\mathrm{anode}}$) and the cathode ($\eta_{\mathrm{conc}}^{\mathrm{cathode}}$) sides, which may give rise to modest voltage losses until the current densities approach the limiting current.

1.2.2.3 Ohmic polarization$(\boldsymbol{\eta}_{\mathbf{ohmic}})$

Ohmic losses occur because of the resistance to the flow of ions in the electrolyte and resistance to flow of electrons through the electrode materials. The dominant Ohmic losses occurs due to ion transport in the electrolyte and can be reduced by decreasing the distance of electrode separation or electrolyte thickness and enhancing the ionic conductivity of the electrolyte.

1.2.2.4 Polarization curve

The polarization curve (Figure 1-4c) shows how SOFC performance is depends on the aforementioned losses. The voltage/current relationship of operational SOFC *E (i)* can be written as

$$E(i) = E_{theoretical} - \eta_{conc}^{anode}(i) - \eta_{conc}^{cathode}(i) - \eta_{act}^{anode}(i) - \eta_{act}^{cathode}(i) - \eta_{ohm}(i) \qquad 1\text{-}8$$

Most importantly, from the polarization curve, it is evident that maximum voltage loss in a SOFC occurs due to the cathode activation polarization. The largest losses occur at the cathode due to the sluggish oxygen reduction reaction (ORR) kinetics (eqn. 1-1). Therefore, understanding of the cathode processes and its catalytic properties is vital to improving the overall performance of the system.

1.3 Solid oxide fuel cell cathodes

The state-of-the-art SOFC cathode is typically made of transition metal oxides (TMO) based material with perovskite crystal structure (ABO_3 type). This class of material is considered attractive due to the low cost, high catalytic activity, selectivity and material tunability [4]. For perovskite, in general, cations with a large ionic radius have twelve-coordination to oxygen atoms and occupy A-sites, and cations with a smaller ionic radius have six-coordination and occupy B-sites (see Figure 1-5). Usually, lanthanides are substituted in A-site and transition metals are substituted in B-site.

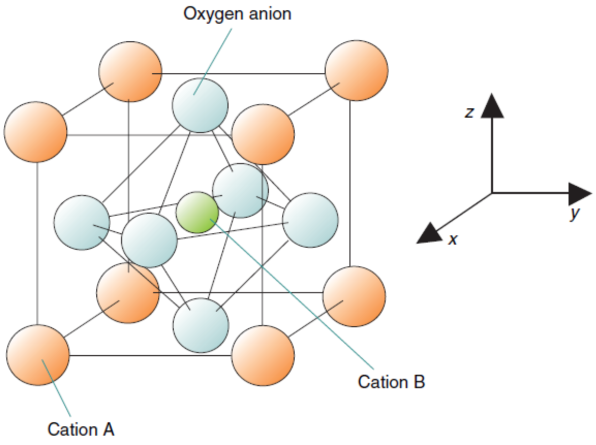

Figure 1-5 Schematic representation of the perovskite structure (ABO_3) (reproduced [25])

1.3.1 Materials for perovskite cathodes

As ORR electrocatalyst (SOFC cathode), perovskite materials should meet certain intrinsic property requirements for adequate performance and stable operation. The most important ones are: electrocatalytic activity, electronic and oxygen ion conductivities, and material stability.

1.3.1.1 Perovskite electrocatalytic activity

Cathode electrocatalytic activity plays the central role in material selection as it has direct relevance to the cathode activation overpotential and, thereby, to the overall cell performance. In the last two decades, significant effort has been directed towards the understanding of the origin of the overpotential for oxygen reduction on transition metals and, subsequently, to design high performance electrocatalysts [9-10]. Recently, similar kind of study reported material design strategies for perovskite-based ORR electrocatalyst [11]. The strategy for increasing the intrinsic electrocatalytic activity is mainly determined by the extent of B-site transition-metal-oxygen covalency and its σ^*-orbital occupation (e_g filling) [11].

In addition to tuning intrinsic electrocatalytic activity, surface area available for electrocatalysis is also an important factor in determining the overall catalytic performance. Perovskite materials usually have small surface areas (<10 m^2/g) due to their high-temperature preparation method (>1073 K). Various attempts to enhance their surface areas were made by changes in the preparation method but the high surface area decreases rapidly at the high temperature of SOFC operation [12].

1.3.1.2 Electronic and ionic conductivity

Electronic and ionic conductivities of perovskite are important factors for material selection as it contributes to Ohmic polarization. Conductive properties of perovskite mainly depend on defect chemistry based on tuning A and B sites [13]. For example, in the case of $Sr_xLa_{1-x}CoO_3$, the Co ions are Co^{3+} for $x = 0$. However, an increase in x (Sr doping) results in the creation of Co^{4+} holes. This drastically changes both electronic and ionic conductivities and shown in Table 1-1.

Table 1-1Perovskite Cathodes: electronic and ionic conductivities in air [taken from 13]

Composition	Temperature (°C)	Electronic conductivity (Scm^{-1})	Ionic Conductivity (Scm^{-1})
$La_{0.6}Sr_{0.4}CoO_3$	800	1,600	0.220
$La_{0.6}Sr_{0.4}FeO_3$	800	129	0.056
$La_{0.8}Sr_{0.2}Co_{0.2}Fe_{0.8}O_3$	800	87	0.022
$La_{0.8}Sr_{0.2}Co_{0.8}Fe_{0.2}O_3$	800	800	0.040
$La_{0.6}Sr_{0.4}Co_{0.8}Fe_{0.2}O_3$	800	269	0.058

1.3.1.3 Material Stability

As a key component of a SOFC unit cell, it is essential for the cathode to be stable over the long-term operation. The stability of perovskite is determined by its lattice structure, valency, and compatibility with contacting materials (cell components and gas stream) [14]. The lattice structure of perovskite is strongly correlated with the Goldschmidt tolerance factor (t) [4].

$$t = \frac{r_A + r_O}{\sqrt{2}(r_B - r_O)} \qquad \text{1-9}$$

If the ionic radii for A, B and O are r_A, r_B and $r_{O,}$ respectively, then to form a perovskite crystal structure, the tolerance factor (t) should lie within the range $0.8 < t < 1.0$, and $r_A >$ 0.090 nm, $r_B >$ 0.051 nm, otherwise, structural distortions appear [4].

Secondly, the relative stability of various valence states of cations and anions affects overall stability of the perovskite structure and reactivity with other chemical species [14]. For example, introducing aliovalent ion into ABO_3 at the A and B sites creates abnormal valences in the perovskite structure and affects its stability and oxygen content. In addition, cathode incompatibility with other contacting phases such as the electrolyte, interconnect, and the inlet gas also causes valence instability and affects its catalytic activity [14].

1.4 Low-temperature solid oxide fuel cell (LT-SOFC)

Lowering the operation temperature of SOFC is a longstanding technology development goal**.** Lowering of the SOFC operation temperature provides various technological and economical advantages due to reduced manufacturing costs (usage of inexpensive construction materials) (Figure 1-6), improved mechanical durability (material degradation caused by the high operating temperatures), and enhanced efficiency of the kW-scale generators. On the other hand, as shown in Figure 1-6, decreasing the operating temperature leads to an increase in the activation polarization seriously affecting the SOFC performance (i.e maximum power density), since the electrochemical reactions and the ionic conductivity are thermally-activated processes.

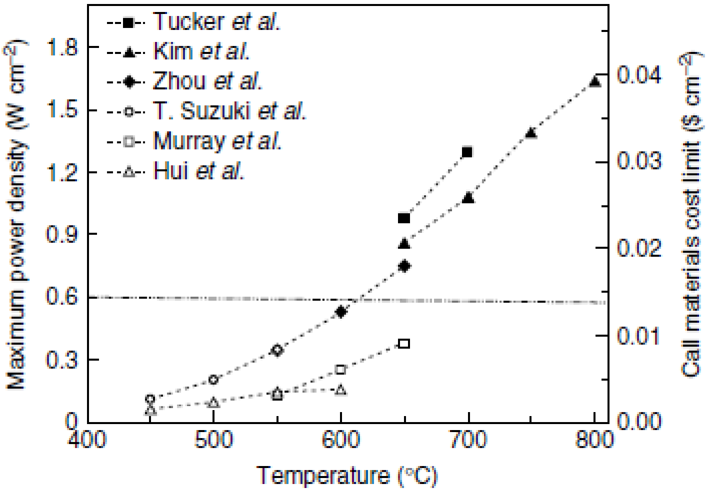

Figure 1-6 Power density and cost of cell materials vs. temperature. (reproduced from [8]).

Thus, a major hindrance to SOFC commercialization relates to lowering the operation temperatures down to 500 °C -700 °C and simultaneously preserving a high performance and durability [15].

1.4.1 Effect of temperature on activation and Ohmic losses

As pointed out earlier, the activation polarization (η_{act}) at electrode/electrolyte represents the voltage loss due to electrochemical reactions. Electrochemical reaction has to overcome activation energy barrier and results in voltage loss required to drive the transfer of the charges between the electronic and ionic phases. The relation between activation polarization $\eta_{act}$and current *(i)* can be represented by Bulter-Volmer equation,

$$i = i_o(e^{\frac{\alpha n F \eta_{act}}{RT}} - e^{-\frac{(1-\alpha) n F \eta_{act}}{RT}}) \qquad 1\text{-}10$$

where, i_o is exchange current density, α is the transfer co-efficient that represents the symmetry of the reaction energy barrier, n is number of electron transferred, R is gas constant and T is temperature. For small values of x, the exponential e^x can be approximated as1 + x. In the same way, under low activation polarization conditions, the Butler-Volmer equation can be linearized to the low-field approximation as:

$$i = i_o \frac{\alpha n F \eta_{act}}{RT} \qquad 1\text{-}11$$

Activation polarization resistance R_p can be correlated to eqn 1-11 as:

$$\frac{1}{R_p} = \frac{i}{\eta_{act}} = i_o \frac{\alpha nF}{RT} \quad \text{1-12}$$

It is important to mention here that exchange current density (i_o) is depend on temperature through Arrhenius type kinetics and equation (1-12) can be modifies as

$$\frac{1}{R_p} = Kexp^{-\frac{E_a}{RT}} \quad \text{1-13}$$

where, K is a function of $\alpha, n, F, R, Tandi_o^{ref}$. And again, ionic conductivity (σ_{ionic}) of electrolyte can be correlated to electrolyte resistance (R_s), Ohmic resistance and temperature as

$$\sigma_{ionic} = \frac{l}{R_s A_e} = \frac{i}{\eta_{ohm}} = \frac{A}{T} exp^{-\frac{E_a}{kT}} \quad \text{1-14}$$

where R_s is the electrolyte resistance, A_e is cross-sectional area for ion transport, l is the electrolyte thickness, A is the pre-exponential factor, k is the Boltzmann constant, and E_a is activation energy. Therefore, from eqn 1-13 and 1-14 and Figure 1-7, it is clearly evident that the activation polarization and Ohmic resistance increases exponentially with a decrease in temperature.

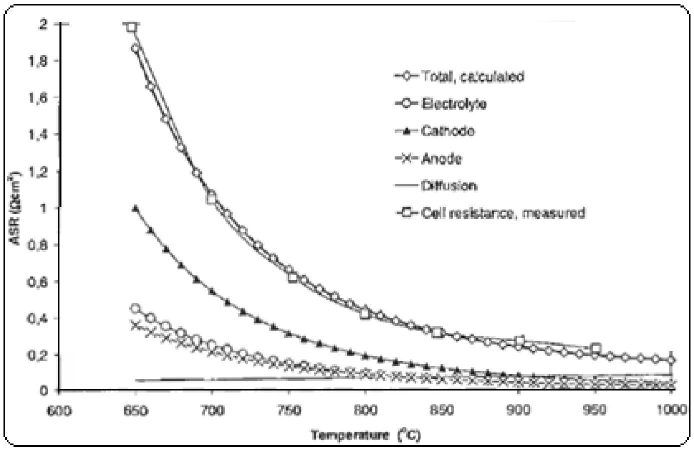

Figure 1-7 Temperature dependence of various polarization resistance of SOFC [reproduced from 4]

Below 700 °C of operation, overall performance of the cell is dominated by cathode overpotential loss or cathode resistance since kinetics of oxygen reduction reaction drastically reduces at lower temperature. Therefore, the development of cathode materials with low polarization resistance is a chief bottleneck in lowering of SOFC operation temperature [15].

1.4.2 Barium-based cathode material for low-temperature SOFCs

Recently, a new class of barium based mixed ionic and electronic conducting perovskite were developed as cathode material for low temperature operation with low area specific resistance (ASR) was reported [16]. Despite the introduction of barium class of materials for SOFC cathodes, few studies have examined the electrocatalytic properties in significant depth. Karan and co-workers [17, 18] examined one specific Ba-based perovskite material- $La_{0.5}Ba_{0.5}CoO_{3-\delta}$ (LBC). They reported very promising catalytic activity with an area specific resistance of only 0.16 Ω-cm^2 at 600 °C. In comparison to one of the most promising low-temperature cathode material $La_{1-x}Sr_xCo_{1-y}Fe_yO_{3-\delta}$ (LSCF), the LBC electrodes were found to have significantly lower electrode resistance than LSCF as shown in Fig 1-8. This indicates that LBC-based cathodes may be preferable over commercial LSCF-based cathodes for lower temperature SOFC operations. Therefore, LBC can be considered as a potential cathode material for Low temperature SOFC (LT-SOFC).

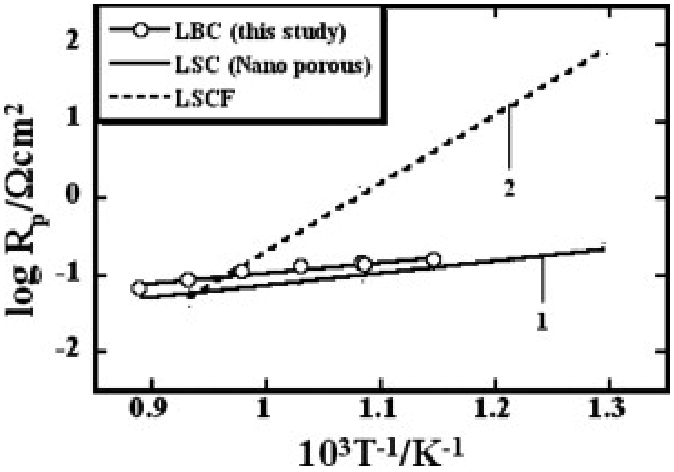

Figure 1-8 Total electrode polarization resistance of LBC electrode is compared with the state-of-the-art low temperature SOFC cathodes such as LSC and $La_{1-x}Sr_xCo_{1-y}Fe_yO_{3-\delta}$ (LCSF) electrodes [reproduced from [17]].

1.5 Thesis motivation

1.5.1 Stability of barium-based-cathodes

Although, LBC was found to exhibit high electrocatalytic activities for ORR in the 550-700°C range, it has been previously reported that perovskite containing alkali earth metals such as barium and strontium are unstable in pure carbon dioxide [19-20] due to the possibility of occurrence of the carbonation reaction.

$$ABO_3 + CO_2 \rightarrow ACO_3 + decomposedphases \qquad 1\text{-}15$$

Therefore, assessment of stability of LBC in carbon dioxide environment became essential since the formation of barium carbonate in LBC cathode will seriously affect the electrocatalytic activity, electronic conductivity and ionic conductivity and in turn overall performance of SOFC.

A specific question that arises is: for SOFC operating temperatures, what level of CO_2 in the air can the LBC cathode tolerate? There are several questions of scientific relevance, not necessarily pertinent to SOFCs that arise: what is thermodynamic phase boundary for carbonate formation during LBC-CO_2 interaction? What products are formed during the LBC-CO_2 interaction? What is the reaction pathway?

1.5.2 The need for rapid testing of multiple electrodes of reproducible features

Although studies comparing electrode performances are commonly reported, very few actually comment on whether the differences are statistically significant. Cell-to-cell or electrode-to-electrode performance variability is seldom reported. Performance variability can arise due to the lack of or limited control in fabricating electrodes of reproducible micro structural (pore size and particle distributions) or even macroscopic features (similarity and uniformity of thickness) by conventional fabrication methods. Lack of reporting of reproducibility of electrode performance partially arises from the fact that testing of a single electrode can be a time-consuming and cumbersome process. Some factors that deter experimentalists from carrying out testing on multiple samples are time and care required for setting up an experiment (e.g. connecting and disconnecting the electrical contacts) as well as time required for bring the electrode to high temperature and then cool it down.

Thus, a test system for characterizing the electrochemical performance of multiple electrodes rapidly would be beneficial. Furthermore, there is a need for development of methods for fabricating reproducible electrodes. Addressing these two important issues are the major motivation behind my thesis work. This is because material development research can be accelerated by creation of material libraries with varying properties and testing the large set of materials using reliable and fast approach [21-23].

1.6 Thesis objective

As mentioned above, my research thesis particularly focuses on two distinct but related objectives:

1. To study the stability of newly developed barium-based cathode material ($La_{0.5}Ba_{0.5}CoO_{3-\delta}$) in the presence of carbon dioxide atmosphere with specific focus on the thermodynamics and decomposition mechanism for the carbonate formation.
2. Development of a test system for rapid testing of multiple electrodes. An associated goal was to develop protocol for fabrication of millimeter or smaller size electrodes by inkjet printing technique.

1.7 Organization of thesis

The thesis is organized in a manuscript style format. Chapter 2 deals with the study of LBC reaction with CO_2. Through a combination of thermogravimetry experiments, ex-situ X-ray diffraction (XRD) of reacted material, and high temperature in-situ X-ray diffraction (HT-XRD),the LBC perovskite material stability, decomposition pathway and carbonation kinetics were investigated. Chapter 3 discusses the details of microelectrode fabrication through inkjet printing, calibration of test system and demonstration of proof of concept for rapid testing of multiple electrodes.

1.8 References

1) Bhattacharyya, S. C. In *Energy Economics: Concepts, Issues, Markets and Governance;* Springer Verlag: 2011; *BP energy outlook 2030.* BP: London, 2011.

2) Barbaro, P.; Bianchini, C. *Catalysis for sustainable energy production;* Wiley-VCH ; John Wiley distributor]: Weinheim; Chichester, 2009.

3) *BP energy outlook 2030.* BP: London, 2011.

4) Singhal, S. C.; Kendall, K. *High temperature solid oxide fuel cells: fundamentals, design, and applications;* Elsevier Science: 2003.

5) Wachsman, E. D.; Marlowe, C. A.; Lee, K. T. Role of Solid Oxide Fuel Cells in a Balanced Energy Strategy. *Energy Environ.Sci.* **2011**, *5*, 5498-5509.

6) Leonide, A. SOFC modelling and parameter identification by means of impedance spectroscopy, KIT Scientific Publishing, Karlsruhe, 2010.

7) Chan, S. H.; Khor, K. A.; Xia, Z. T. A Complete Polarization Model of a Solid Oxide Fuel Cell and its Sensitivity to the Change of Cell Component Thickness. *J. Power Sources* **2001**, *93*, 130-140.

8) Vielstich, W.; Lamm, A.; Gasteiger, H. A.; Yokokawa, H. In *Handbook of fuel cells : fundamentals, technology, and applications;* Wiley: Chichester, England; Hoboken, N.J., 2003.

9) Stamenkovic V; Mun BS; Mayrhofer KJ; Ross PN; Markovic NM; Rossmeisl J; Greeley J; Nørskov JK Changing the Activity of Electrocatalysts for Oxygen

Reduction by Tuning the Surface Electronic Structure. *AngewandteChemie (International ed.in English)* **2006**, *45*, 2897-901.

10) Norskov, J.; Rossmeisl, J.; Logadottir, A.; Lindqvist, L.; Kitchin, J.; Bligaard, T.; Jonsson, H. Origin of the Overpotential for Oxygen Reduction at a Fuel-Cell Cathode RID A-5714-2011 RID A-2363-2010 RID A-6161-2011. *J PhysChem B* **2004**, *108*, 17886-17892.

11) Suntivich, J.; Gasteiger, H. A.; Yabuuchi, N.; Nakanishi, H.; Goodenough, J. B.; Shao-Horn, Y. Design Principles for Oxygen-Reduction Activity on Perovskite Oxide Catalysts for Fuel Cells and Metal-Air Batteries. *Nature Chemistry* **2011**, *3*, 546-550.

12) Tanaka, H.;Misono, M. Advances in Designing Perovskite Catalysts. *Current Opinion in Solid State &Materials Science***2001**, *5*, 381-387.

13) Sun, C.; Hui, R.; Roller, J. Cathode Materials for Solid Oxide Fuel Cells: A Review RID A-9860-2008. *Journal of Solid State Electrochemistry* **2010**, *14*, 1125-1144.

14) Yokokawa, H. Understanding Materials Compatibility. *Annual Review of Materials Research* **2003**, *33*, 581-610.

15) Wachsman, E. D.; Lee, K. T. Lowering the Temperature of Solid Oxide Fuel Cells. *Science* **2011**, *334*, 935-939.

16) Shao, Z.; Haile, S. M. A High-Performance Cathode for the Next Generation of Solid-Oxide Fuel Cells. *Nature* **2004**, *431*, 170-173.

17) Amin, R.; Karan, K. Characterization of $La_{0.5}Ba_{0.5}CoO_{3\text{-delta}}$ as a SOFC Cathode Material. *J. Electrochem. Soc.* **2010**, *157*, B285-B291.

18) Amin, R.; Kenney, B.; Karan, K. Characterizations of LBC-GDC Composite Cathodes for Low Temperature SOFCs. *J. Electrochem. Soc.* **2011**, *158*, B1076-B1082.

19) Ryu, K. H.; Haile, S. M. Chemical Stability and Proton Conductivity of Doped $BaCeO_3$-$BaZrO_3$ Solid Solutions. *Solid State Ionics* **1999**, *125*, 355-368.

20) Zakowsky, N.; Williamson, S.; Irvine, J. T. S. Elaboration of CO2 Tolerance Limits of $BaCe_{0.9}Y_{0.1}O_{3\text{-Delta}}$ Electrolytes for Fuel Cells and Other Applications. *Solid State Ionics* **2005**, *176*, 3019-3026.

21) Potyrailo, R. A.; Rajan, K.; Stowe, K.; Takeuchi, I.; Chisholm, B.; Lam, H. Combinatorial and High-Throughput Screening of Materials Libraries: Review of State of the Art. *ACS Combinatorial Science* **2011,***6*, 579–633.

22) Baerns, M.; Holeňa, M. In *Combinatorial development of solid catalytic materials: design of high-throughput experiments, data analysis, data mining;* Imperial College Press: 2009; Vol. 7.

23) Potyrailo, R. A.; Maier, W. F. In *Combinatorial and high-throughput discovery and optimization of catalysts and materials;* CRC Taylor & Francis: Boca Raton, FL, 2007.

24) http://www.netl.doe.gov/technologies/coalpower/fuelcells/seca/primer/cell.html (accessed 03/01, 2012).

25) https://www.nttreview.jp/archive/ntttechnical.php?contents=ntr200709sp1.html (accessed 03/01, 2012).

26) Menzler, N. H.; Tietz, F.; Uhlenbruck, S.; Buchkremer, H. P.; Stöver, D. Materials and Manufacturing Technologies for Solid Oxide Fuel Cells. *J. Mater. Sci.* **2010**, *45*, 3109-3135.

Chapter 2

Carbonate Formation in $La_{0.5}Ba_{0.5}CoO_{3-\delta}$ (LBC) - Carbon dioxide System: Reaction Pathway, Kinetics and Thermodynamics

2.1 Introduction

Lowering of the operating temperature to 500° C – 700° C range is a long-term goal of solid oxide fuel cell (SOFC) system development [1]. Low temperature operation allows the usage of cheaper material of construction, ensures quick start up / shutdown procedure, and reduces the degradation of cell components [2]. However, lower temperature implies significant penalty in the cell performance since both the electrochemical reaction and ionic conduction are thermally-activated processes. In fact, below 700 °C of operation, the overall cell performance is dominated by the cathode overpotential. Thus, designing cathode material with minimal loss is one of the key goals of the low-temperature SOFC (LT-SOFC) development [3]. Therefore, development of new cathode materials exhibiting higher oxygen reduction activity are being pursued [4].

Recently, a new class of cathode material based on barium containing perovskite that is a mixed ionic-electronic conductor (MIEC) has been reported for LT-SOFC application [5-7]. Our group examined a specific perovskite, $La_{0.5}Ba_{0.5}CoO_{3-\delta}$ (LBC), and found the area specific resistance (ASR) for the electrode to be as low as 0.16 Ω-cm^2 at 600°C in air at open circuit voltage condition.

However, alkali earth metals such as barium- and strontium-substituted perovskite compounds are unstable in carbon dioxide atmosphere due to alkali carbonate formation [8-17]. Because of this concern, alkali earth metal based proton-conducting perovskite, oxygen separating MIEC-perovskite, and high-temperature superconducting perovskite were extensively investigated for stability in carbon dioxide atmosphere [8-11]. Theoretical studies have focused on the thermodynamic calculation for phase stability and experimental studies have investigated carbonation/de-carbonation kinetics of barium-based perovskite [10-15]. In addition, high-temperature in-situ x-ray diffraction (HT-XRD) measurements were performed under carbon dioxide atmosphere to study the perovskite phase/structural transformation during carbonation process and have provided insights on reaction pathway as well as the material stability [15-18].

In case of SOFC cathode perovskite, ambient air could be fed at the cathode side, which can contain low but significant level of CO_2 - 380 ppm. Since, carbonation of perovskite can seriously affect its electrocatalytic and conductive properties, studies of carbon dioxide effect on barium-based SOFC cathode are critical for long-term stability. Initial studies on the phase stability and electrocatalytic activity of $Ba_{0.5}Sr_{0.5}Co_{0.2}Fe_{0.8}O_3$(BSCF) based single cell shown significant deterioration of oxygen reduction kinetics in the presence of low CO_2 partial pressure (0.28%) even at 450 °C [19, 20]. In our group, a complete loss in the activity was reported for LBC electrode exposed to pure CO_2 atmosphere overnight at 700^{o}C [6]. From the aforementioned discussions, it can be concluded that an investigation on LBC stability in the presence of carbon dioxide atmosphere is much needed.

In the present work, we examine the LBC-CO_2 reaction system by a combination of thermogravimetry analysis (TGA), ex-situ X-Ray Diffraction (XRD) of products and in-situ high-temperature XRD (HT-XRD) of the reacting system. The TGA measurements generated mass change data whereas XRD analyses allowed the identification of new solid-phase products formed. TGA measurements allowed the determination of the onset temperature of carbonate formation and ultimately the determination of fundamental standard state thermodynamic parameters, viz. ΔH^{o} and ΔS^{o}, for the carbonate formation reaction. By combining TGA analysis with XRD analyses, reaction stoichiometries could be ascertained and allowed identification of reaction pathways. Finally, it was found that a simple homogeneous kinetic model adequately described the kinetics of carbonate formation.

2.2 Experimental section

2.2.1 Material preparation

$La_{0.5}Ba_{0.5}CoO_{3-\delta}$ (LBC) was synthesized using solid-state synthesis route as described in previous work from our group [6, 7]. Briefly, the synthesis method involved mixing of required amounts of lanthanum and cobalt oxide (Alfa Aesar, 99.9% purity) and barium carbonate (Alfa Aesar, 99.8% purity) powder, grinding or an hour, pelletization of resulting powder mixture into 13 mm diameter disk by applying a load of 153 MPa, followed by calcining the pellet at 1000°C for 12 h in air, and a final step in which the calcined pellet was ground, re-pelletized, and heat-treated at 1150°C for 24 h in air. The phase purity of prepared LBC material was ascertained by XRD analysis.

2.2.2 Thermogravimetric analysis (TGA)

Thermogravimetry analysis of LBC under various CO_2 partial pressures (100%, 5%, 2%, and 1% of $CO_2$by volume in CO_2/N_2 mixture) was performed using TGA (Q500 V6.7 Build 203, TA instruments). Purge gas of desired CO_2 partial pressure (Praxair, 99.9%) was supplied to TGA chamber with the flow rate of 40.0 ml/min. Approximately, 50 mg of sample was spread on the bottom of platinum sample pan for each measurement. Two different types of TGA experiments were carried out – (i) non-isothermal TGA and (ii) isothermal TGA. The protocols for these experiments are described in the following two sub-sections.

2.2.2.1 Non-isothermal Thermogravimetry (NI-TGA)

Non-isothermal TGA experiments were performed to specifically determine the carbonation reaction onset point and to follow reaction progress during temperature scan measurements. Two types of NI-TGA experiments were carried out referred to as the heating and the cooling experiments. In both experiments, the sample was heated from room temperature to a specified set point temperature, held at the set point temperature for a specified time and then cooled back to room temperature. The differences occur with respect to when the CO_2 is introduced during the heating-hold-cooling cycle as described in this section. The onset of carbonate formation during heating experiment is deemed to be kinetic activation of reaction whereas that during the cooling experiment is representative of the thermodynamic boundary for carbonate formation.

Heating Experiments: During the heating experiment, as shown in Figure 2.1, pure carbon dioxide atmosphere was maintained throughout the heating-hold-cooling cycle and the mass change recorded continuously. The sample was heated from 30 °C to 900 °C at a specified heating rate (2 °C/min),maintained isothermally at 900°C for 60 minutes, and finally, cooled down to room temperature in the same atmosphere.

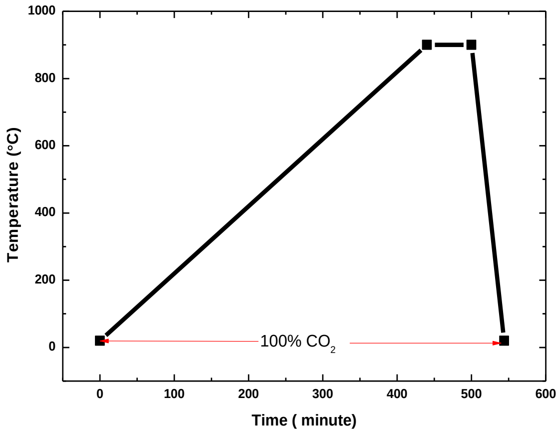

Figure 2-1 Temperature profile for non-isothermal TGA heating experiment

Cooling Experiments: In the case of cooling experiments, as shown in Figure 2.2, the sample temperature was raised to 1000°C in nitrogen atmosphere, soon after reaching 1000°C the chemical environment was switched to gas mixture of known carbon dioxide partial pressure and the system allowed to equilibrate for short period (60 minutes) and, finally, the sample is cooled at a specified cooling rate in the CO_2 environment. Experiments at different cooling rates were carried out. Faster cooling rate (2^{o}C/min) were done to ascertain whether a carbonate formation onset was observable for the given CO_2 partial pressure. If an onset point was observed, experiments at a slower cooling rate (0.3^{o}C/min) were performed to determine a carbonate formation onset temperature that is thermodynamically meaningful.

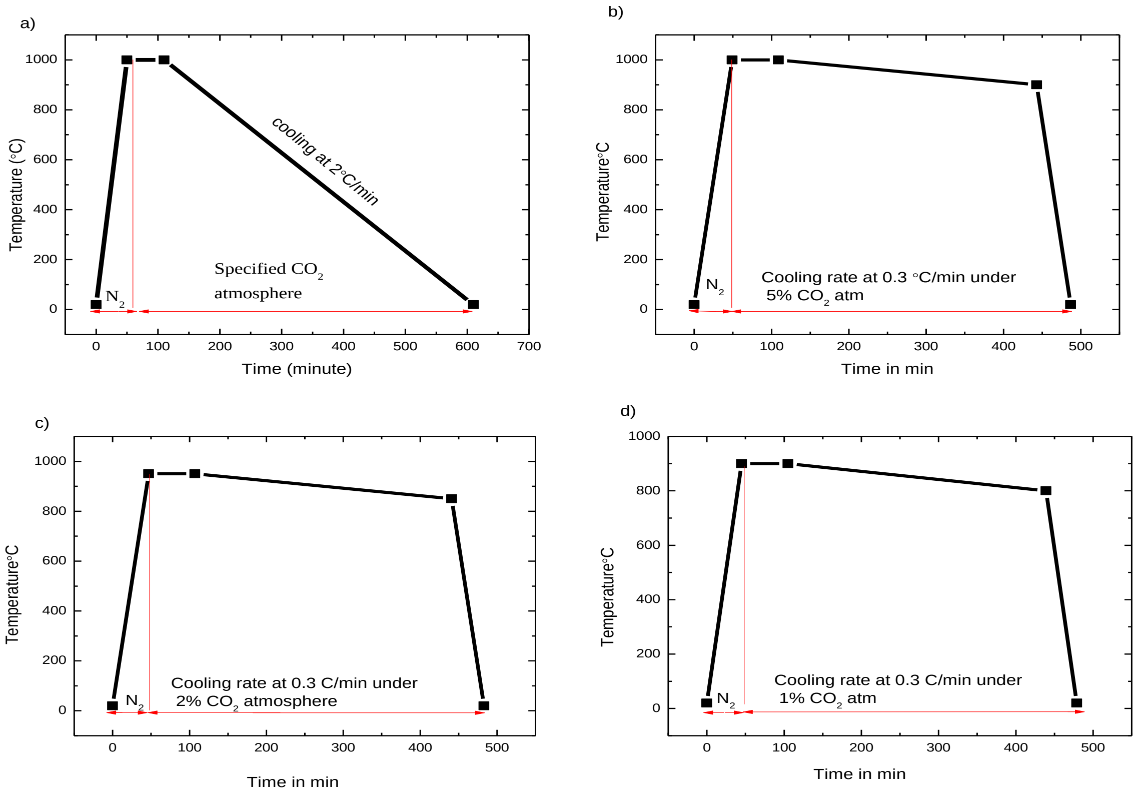

Figure 2-2 Temperature profile for cooling experiment (a) at faster scan (2^{o}C/min) and (b),(c),(d) for slow scan method in a short interval of temperature range for 5mol%,2mol% and 1mol% CO_2 in CO_2-N_2 mixture, respectively.

2.2.2.2 Isothermal Thermogravimetry

Isothermal TGA experiments were performed to study the kinetics of carbonate formation at a specific temperature and find the ultimate mass change upon completion of the reaction. For the isothermal measurements, the LBC sample was heated to a desired set point temperature at the rate of 20 °C/min under a nitrogen atmosphere. Then, the material was maintained in the same atmosphere to stabilize (for 120 min). Subsequently, the chemical environment was switched from nitrogen to pure carbon dioxide atmosphere to study carbonation reaction kinetics and cooled in same atmosphere (20 °C/min). The temperature profile and changes in the chemical environment during the experiment is depicted in Figure 2-3 below.

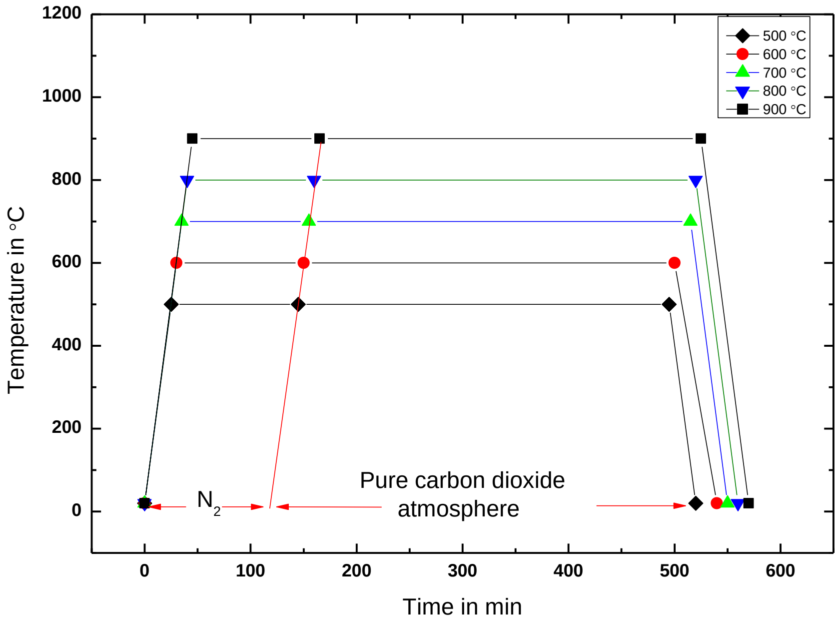

Figure 2-3 Temperature profile for Isothermal TGA experiments

2.2.3 Ex-situ X-ray Diffraction Studies (XRD)

The solid-phase material remaining at the end of the TGA experiments, hereafter referred to as the post-TGA samples, were carefully collected for phase analysis. The post-TGA as well as the as-prepared (un-reacted) LBC samples was analyzed using XRD to determine the various phases with a PANalyticalX'Pert Pro MPD diffractometer fitted with an X'Celerator high speed strip detector. Samples were mounted as thin smears of fine powder on glass disks. Copper Kα radiation (Ni filtered) was used with a count time of 2.5 sec at 0.02º steps, 2θ increments were scanned from 10º to 80º at a rotation of 2 sec/revolution.

2.2.4 High temperature In-situ X-ray diffraction studies (HT-XRD)

Selected high-temperature in-situ XRD (HT-XRD) experiments were carried out in Prof. V. Thangadurai's group (Department of Chemistry, The University of Calgary) by his graduate student Wang Hay Kan. These measurements allowed the monitoring of the evolution of solid phase products during the reaction. Bruker D8 Advance Powder X-ray Diffractometer (PXRD) (40 kV, 40 mA) (Cu K_α) equipped with high temperature reactor chamber (Anton Paar XRK 900) was used for in-situ XRD analysis. The diffractogram were collected 2 θ from 10 to 80^o with step size = 0.05 º. PANalytical HighScore software (2009 version) was used for phase identification. For phase identification, the software compares the peak positions and peak intensities for the sample against the large database of known phases.

Two types of experiments were performed – (i) non-isothermal experiments with isothermal XRD scan at different temperature (ii) isothermal experiments with XRD scan at regular intervals. The temperature profiles during the experiments and the pertinent details are presented below.

Non-isothermal high temperature in-situ XRD (HT-XRD) experiments: These experiments were carried out to monitor the phase changes of LBC in pure (100%) carbon dioxide in the temperature range of 30-900 °C. For non-isothermal HT- XRD measurements, LBC sample was exposed to pure carbon dioxide atmosphere at room temperature and the temperature was then increased in steps of 100 °C, from 400 °C to 900 °C. At each set temperature, sample was allowed to stabilize for 5 minutes and XRD was measured (Figure 2-4).

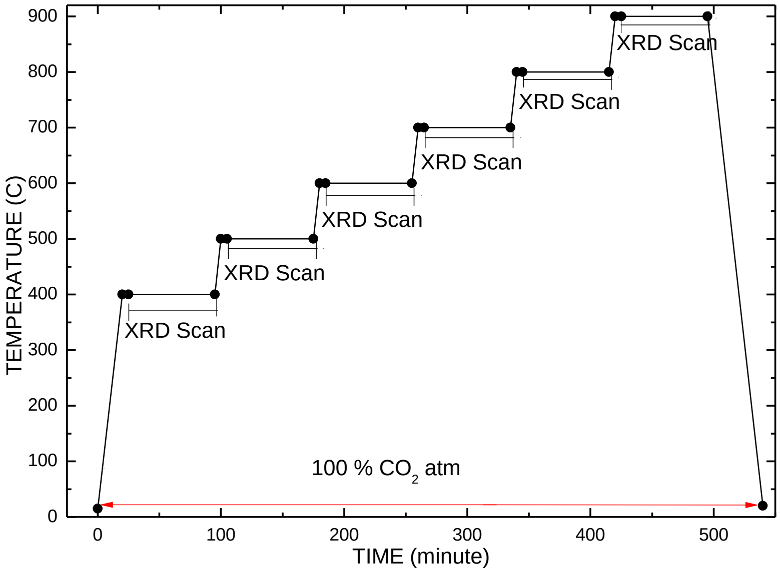

Figure 2-4 Temperature profile and scan interval for non-isothermal HT XRD studies

Isothermal HT-XRD experiments: These experiments were carried out by the first heating the material in nitrogen atmosphere to a set point temperature, stabilizing for 2 hours at set point temperature, and finally changing the nitrogen environment to carbon dioxide environment at the set-point temperature.XRD scans was taken every 20 minutes for 3 hours. Finally, the sample was cooled down to room temperature.

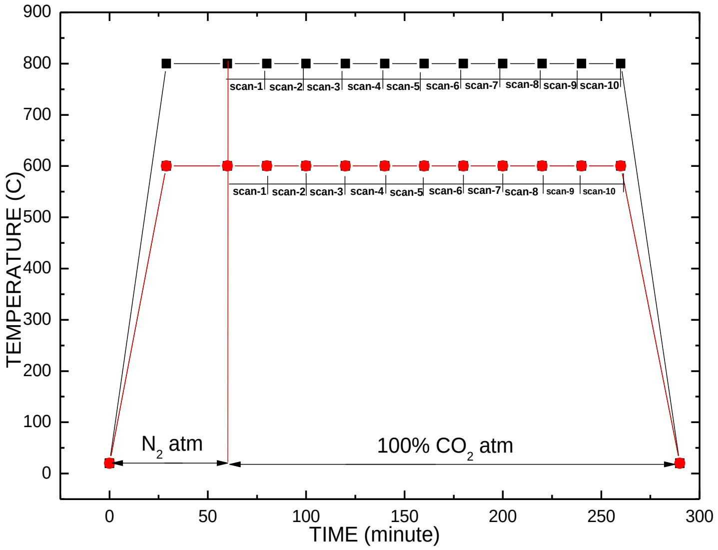

Figure 2-5 Temperature profile and scan interval for isothermal HT-XRD studies

2.3 Results and Discussions

Prior to discussing the results of the experiments, it is important to understand the general aspects of the carbonate formation reaction. Carbonates of alkali metal oxides are unstable at higher temperature, decomposing into metal oxide and

CO_2 (eg.$BaCO_3 \rightarrow BaO + CO_2$). Thus, a mixture of alkali metal oxides and CO_2 will be stable at temperatures higher than the thermodynamic phase boundary temperature [14-15]. On the other hand, such a mixture would thermodynamically be favored to react and form carbonate at lower temperatures (see figure 2-6).

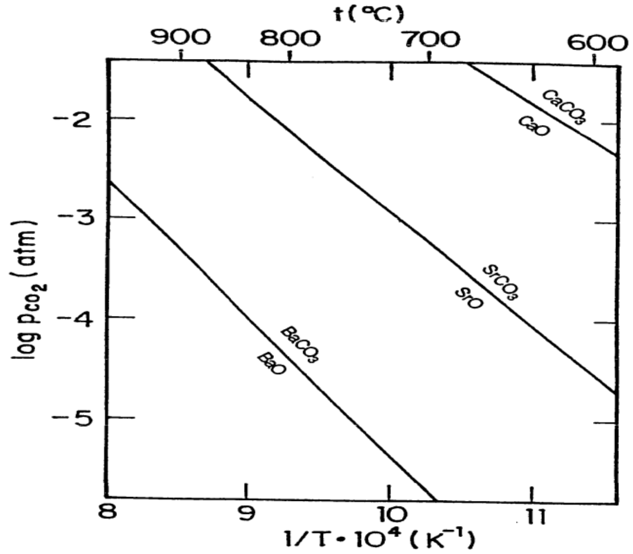

Figure2-6 Thermodynamic phase boundary of carbonate formation (reproduced from [33])

It is important to mention here that at room temperature, no appreciable reaction would proceed due to kinetic limitation and as such carbonate formation will not be observed. However, if such a mixture is heated the kinetics of the reaction become appreciable at some temperature and carbonate formation would start. However, this onset temperature for carbonate formation is a kinetics phenomenon and distinct from the thermodynamic onset temperature, i.e. the temperature defining the carbonate phase boundary [11]. To detect the thermodynamic onset temperature, it would be necessary to approach the phase boundary from higher temperature where the oxide and CO_2 are stable and slowly cool down the mixture until the carbonate formation is detected.

The first half of the results and discussions (section 2.3.1) is concerned with experiments conducted at temperatures below the thermodynamic onset conditions. The reaction pathway and the kinetics of the carbonate formation are investigated. The second half of the results and discussions (section 2.3.2) is concerned with the thermodynamic phase boundary of the reaction.

2.3.1 Reaction of LBC with CO_2

2.3.1.1 Non-isothermal Experiments

This sub-section discusses reaction progress when a LBC sample is heated from room temperature to 900°C in the presence of CO_2. Figure 2-6 presents the TGA data collected during the heating of LBC from room temperature to 900°C at 2°C/min, 60 minutes hold at 900°C and rapid cooling in pure CO_2 atmosphere. Figure 2-7(a) presents the mass changes versus temperature data whereas Figure 2-7 (b) shows the temperature and mass profile as a function of time. Several interesting features in the gravimetric profile can be noted. First, a gentle drop in mass occurs between 150°C and 500°C. A sharp increase is observed around 550°C which continues until approximately 725°C followed by slow-down and drop in the 725 -750 °C ranges. A further increase in mass change between 750°C and 850 °C followed by a significant mass decrease can be noted as the samples continues to be heated and held at 900 °C. Finally, a small increase in mass during the rapid cooling period is observed.

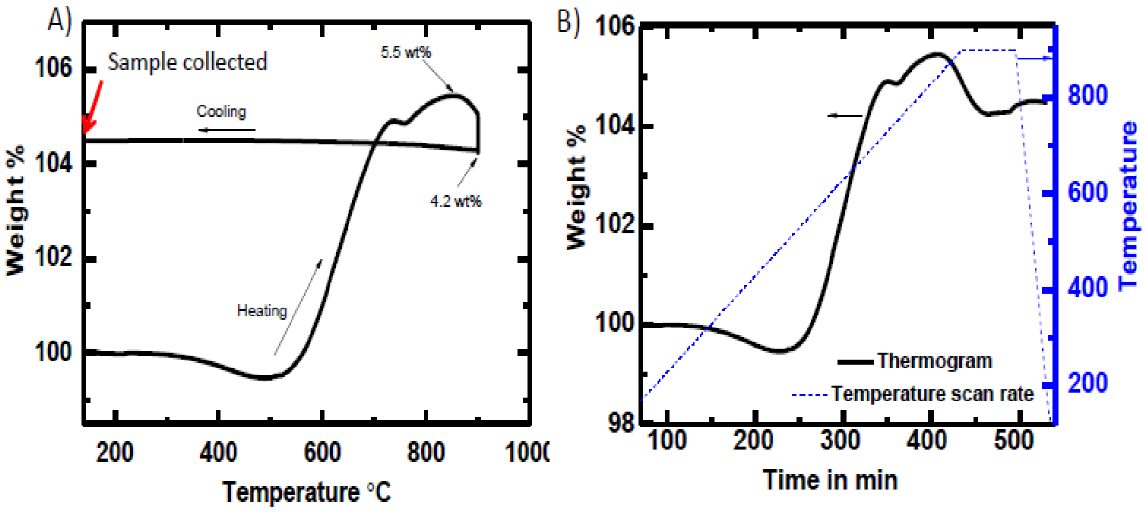

Figure 2-7 Non isothermal TGA of LBC in 100 % CO_2 atmosphere scanned at a heating rate of 2°C/min from 30°C to 900°C and maintained isothermally at 900°C for 60 min prior to cooling down to 30°C at the rate of 20°C/min (A) weight change as a function of temperature B) weight change and temperature change as a function of time

Although the TGA data of Figure 2-7 does not lend itself to analysis of the chemistry of reaction, the initial mass loss and the onset of mass gain can be attributed to the loss of oxygen content from the perovskite and the initiation of carbonation reaction, respectively. It is known that the equilibrium concentration of oxygen content (oxygen non-stoichiometry, δ) in LBC is a function of temperature and oxygen partial pressure (PO_2) of reacting atmosphere [21-24]. Since the surrounding gas (pure CO_2) has very low pO_2 (□2-3 ppm), LBC loses oxygen ($\Delta\delta$) upon an increase in the temperature. The mass increase of the solid LBC sample can occur only by interaction(s) with the only other material species in the system CO_2, i.e. due to the carbonation reaction.

To gain insight into the reaction of LBC with CO_2, the post-TGA sample was analyzed using XRD. It must be noted that the post-TGA material represents the net change undergone upon heating and cooling of LBC in 100% CO_2 atmosphere. XRD analyses indicated that the major solid phases were: La_2CoO_4, CoO, and $BaCO_3$. The presence of barium carbonate in the post-TGA sample confirmed that the weight increase in thermogram (Figure 2-7) was due to the carbonation of the LBC perovskite. However, ex-situ XRD of the post TGA sample provides information only about the phases at the end of the reaction. Therefore, to understand what occurs between 500 ºC and 900 ºC, in-situ HT-XRD studies in pure CO_2 were performed. The details of the experimental conditions have been presented in section 2.2.4.

The in-situ XRD data as well as the XRD of the post-TGA sample are presented in Figure 2-8. During heating from room temperature to 500 ºC, LBC in pure CO_2 atmosphere retained its original phase and there were no emergence of additional peaks/phases.

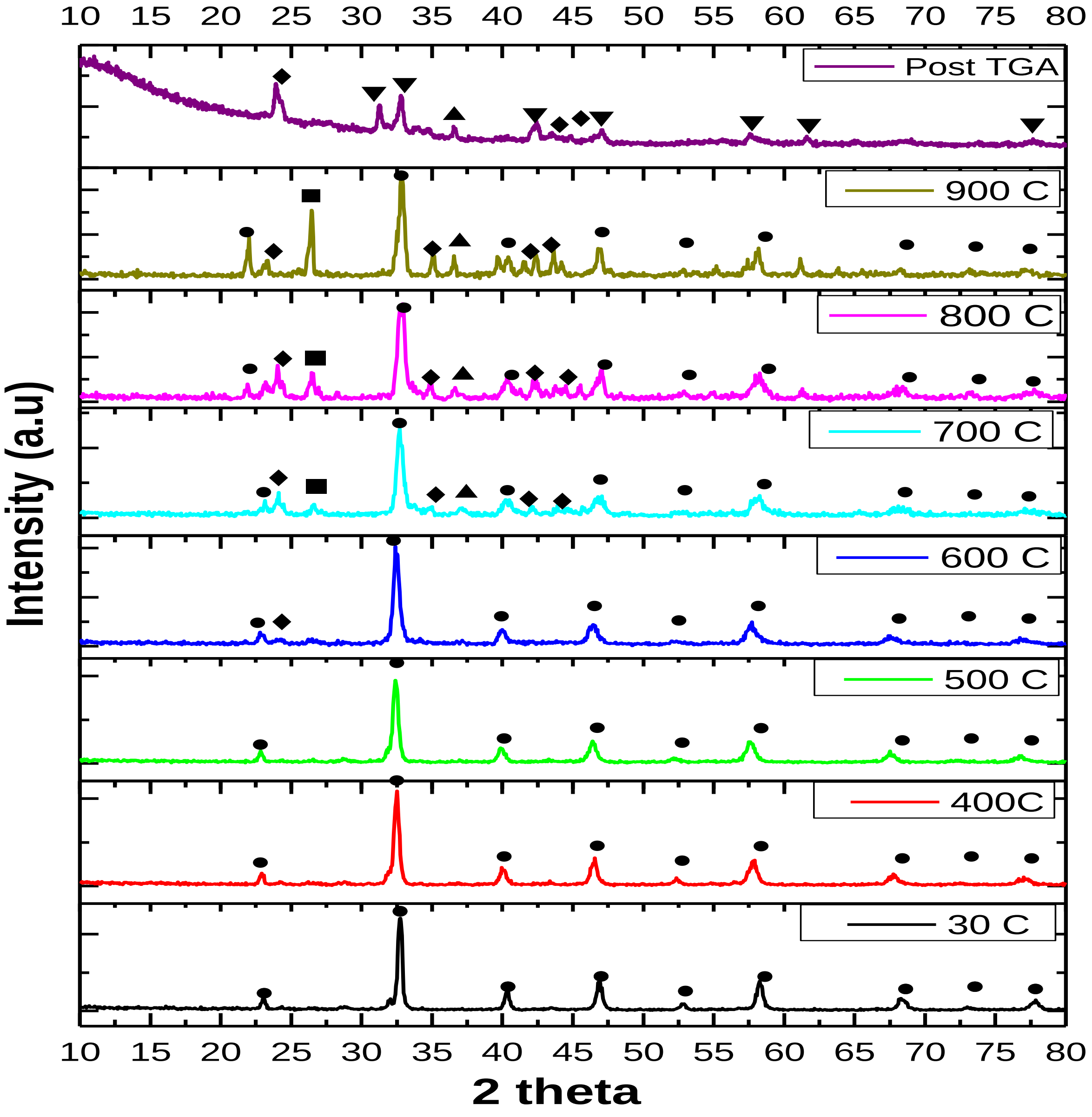

Figure 2-8 Non-isothermal HT-XRD of LBC in 100 % CO_2 ramped in steps of 100 °C, from 400 °C to 900 °C and ex-situ XRD of post TGA sample (phases are ●-LBC/$LaCoO_3$ ♦- $BaCO_3$(ortho) ■-$BaCO_3$ (rhombo) ▲-CoO ▼- La_2CoO_4).

However, at the next temperature step of 600 ºC, there was clear appearance of new phases namely orthorhombic $BaCO_3$ and CoO with peaks 2θ at 24 and 36.5, respectively. With further temperature increase to 700 ºC, intensity of orthorhombic barium carbonate decreases and new peak appears around $2\theta \approx 26.25$.

New peaks indicate the presence of rhombohedra barium carbonate. Therefore, it can be concluded that orthorhombic barium carbonate is unstable at 700 º C and converts to rhombohedra structure. This is consistent with previous reports that barium carbonate phase transform to rhombohedra around 700 º C and to cubic around 950 º C [9, 16].

$$BaCO_3(\text{orthorhombic}) \xrightarrow{700℃\text{-}900℃} BaCO_3(\text{rhombohedra}) \qquad 2\text{-}1$$

It is important to mention here that LBC and $LaCoO_3$ have similar XRD peak positions and it is not possible to distinguish those using XRD data.

2.3.1.2 Combined analysis of non-isothermal TGA and XRD data

The onset of LBC carbonation reaction (kinetic onset temperature) was observed in the TGA experiment at 550ºC. Consistent with the TGA measurements, in the in-situ HT XRD measurements, carbonate phase was observed at 600ºC but not at 500 ºC. In-situ

HT XRD measurements were not performed at 550ºC. As discussed earlier, between 600ºC and 800ºC, the other solid phases observed were $BaCO_3$ and CoO. Considering these solid phases, the stoichiometry for the overall reaction, between 500 ºC and 800 ºC, can be derived as follows:

$$\mathrm{La_{0.5}Ba_{0.5}CoO_{3-\delta}(s)} + \frac{1}{2}\mathrm{CO_2(g)} \xrightarrow{500-800℃} \frac{1}{2}\mathrm{LaCoO_3(s)} + \frac{1}{2}\mathrm{CoO(s)} + \frac{1}{2}\mathrm{BaCO_3(s)} + \frac{1-2\delta}{4}\mathrm{O_2(g)} \quad \text{2-2}$$

The net mass change upon completion of reaction as per the stoichiometry of reaction (2-1) can be calculated if the oxygen non-stoichiometry (δ) is known. Unfortunately, the initial oxygen non-stoichiometry of the LBC (δ) is not known, although it is expected to vary between 0 and 0.25. If the initial LBC oxygen non-stoichiometry is considered as negligible ($\delta \approx 0$), upon completion of reaction as per eqn 2-1, theoretically a mass increase of 5.7 wt% can be calculated. This compares well with the maximum mass change of 5.5 wt% observed during the TGA experiment (see Figure 2-7).

Further, upon comparing in-situ HT XRD data at 900 ºC with the post-TGA ex-situ XRD data, La_2CoO_4 is found to be in the post-TGA sample but not in in-situ XRD sample (900ºC) in which $LaCoO_3$ phase was identified. It must be recalled that the post-TGA sample was held at 900ºC for 60 minutes during which it undergoes mass loss. On the other hand, the in-situ HT XRD data was obtained for sample that had spent 20 minutes at 900ºC. Thus, it can be argued that during the isothermal hold conditions at 900ºC, the perovskite product phase undergoes a transformation from simple cubic ($LaCoO_3$) to layered structure (La_2CoO_4).Similar phase transformation ($LaCO_3 \rightarrow La_2CoO_4$) at high temperature under reducing atmosphere has been reported [25-27]. As such, the reaction undergoing at isothermal condition at 900 ºC (Figure 2-7) can be written as:

$$LaCoO_3 \xrightarrow{900\ ^{\circ}C} \frac{1}{2}\mathrm{La_2CoO_4} + \frac{1}{2}\mathrm{CoO} + \frac{1}{4}\mathrm{O_2} \uparrow \qquad 2\text{-}3$$

Again, from the stoichiometry of reaction (2-3) a mass change of 1.63 wt% would occur. This change is in reasonable agreement with the NI-TGA data (Figure 2-7) wherein a weight decrease of 1.25 wt % (from 5.5 wt % to 4.25 wt %) is observed. It is important to point out that the theoretical weight change value mentioned here have uncertainty associated with it, since the initial LBC oxygen non-stoichiometry (δ) may vary approximately between 0 and 0.25 based on synthesis condition and methods [31].

From the combined TGA and XRD analysis, a reaction pathway as shown in Figure 2-9 is proposed to occur.

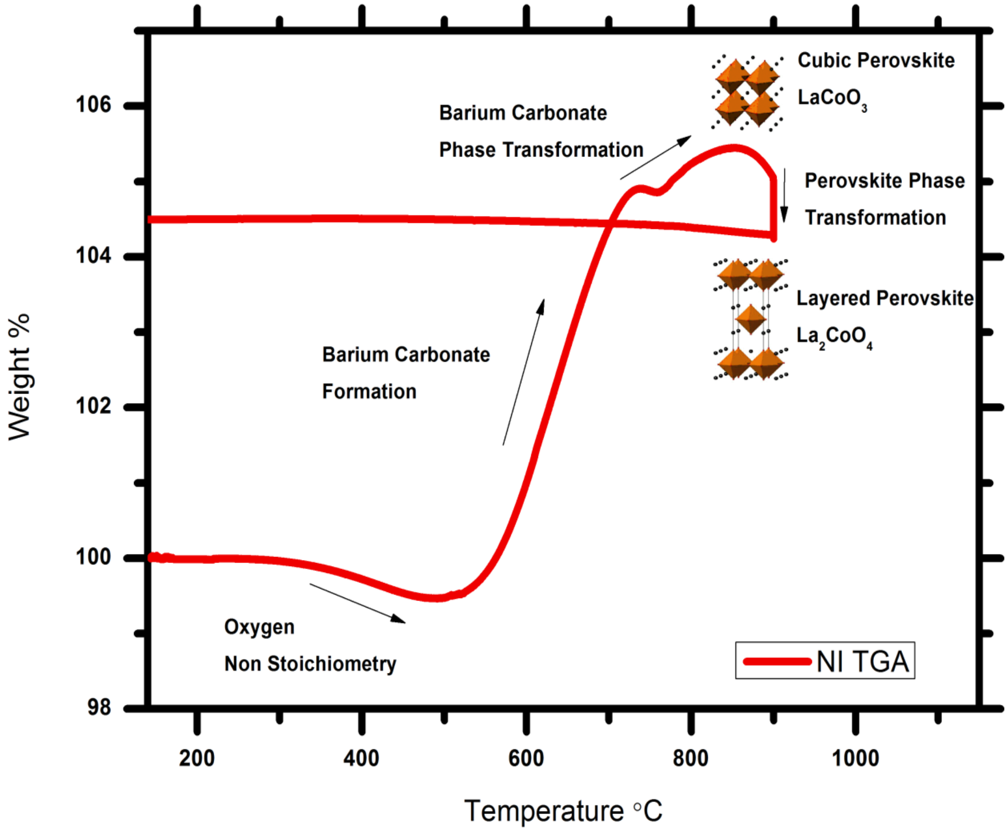

Figure 2-9 Proposed LBC reaction pathway in pure CO_2 atmosphere during heating experiment. (Perovskite structure shown in the schematic were taken from [34])

2.3.1.2 Isothermal studies

Isothermal TGA (I-TGA) experiments at different temperatures were carried out to further understand the LBC-CO_2 reaction. The samples were brought to the set point temperature in nitrogen atmosphere and allowed to stabilize for 120 minutes prior to changing the gas environment from N_2 to CO_2.The TGA results of these experiments are shown in Figure 2-10. For all experiments an initial mass loss, prior to the introduction ofCO_2, was observed and was attributed to oxygen loss from the LBC. Whereas this initial loss at lower temperatures (500°C-800°C) seem to stabilize during the hold period, for the 900º C experiment a continued loss of mass (oxygen) was observed.

From Figure 2-10, it can be noted that upon the introduction of CO_2, for higher temperature experiments (700 ºC, 800ºC and 900ºC) a rapid mass change occurs reaching a steady-state value. At 600 ºC, the mass increase is slower but a steady-state value is reached after 6 hours. On the other hand, at 500ºC the kinetics of mass increase (carbonation) was very slow and a continuous slow increase in mass can be observed even after 6 hours.

One of the most interesting observations that can be made from Figure 2-10 is that for experiments at 600 ºC, 700 ºC, and 800 ºC, a steady-state weight change of 5.1 wt% is observed whereas that at 900ºC a steady-state weight change of 4 wt% is observed. The reacted products (post TGA sample) were examined using XRD to identify the existing solid phases (Figure 2-11).Major phases after the decomposition between 500 ºC and 800 ºC were orthorhombic barium carbonate ($BaCO_3$), lanthanum cobaltite ($LaCoO_3$) and cobalt oxide (CoO).Therefore, it can be confirmed again that equation 2-2 is valid in the region 500-800 ºC under pure carbon dioxide atmosphere.

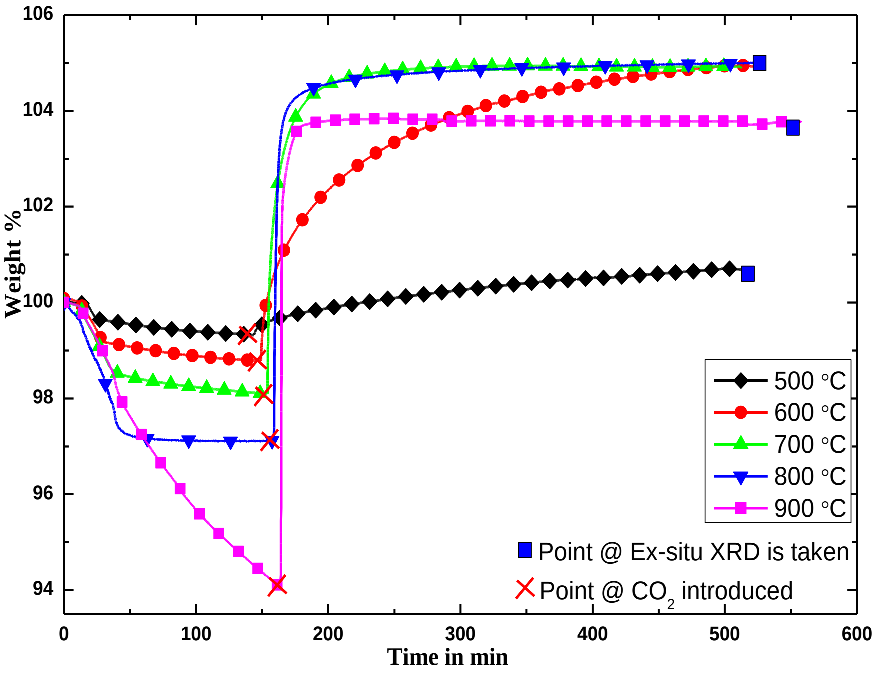

Figure 2-10 Isothermal TGA of LBC in 100 % CO_2 atmosphere where LBC is stabilized at specified temperate in N_2 for 2 hours followed by the introduction of pure CO_2

The products from the 900 °C experiment were found to be La_2CoO_4, CoO, and orthorhombic $BaCO_3$, similar to those found during the non-isothermal experiments discussed in section 2.3.1.1 Therefore, the overall reaction that occurs during the isothermal experiment at 900°C can be written by combining reaction 2-2 and 2-3 as follows:

$$La_{0.5}Ba_{0.5}CoO_{3\text{-}\delta} + \frac{1}{2}CO_2 \xrightarrow{900\ ^\circ C} \frac{1}{4}La_2CoO_4 + \frac{1}{2}BaCO_3 + \frac{3}{4}CoO + \frac{1.5\text{-}2\delta}{4}O_2\uparrow \qquad 2\text{-}4$$

Whether La_2CoO_4 forms directly during the experiment or whether $LaCoO_3$ is formed followed by immediate decomposition into La_2CoO_4 as per reaction 2-3 cannot be ascertained from the data in the current study.

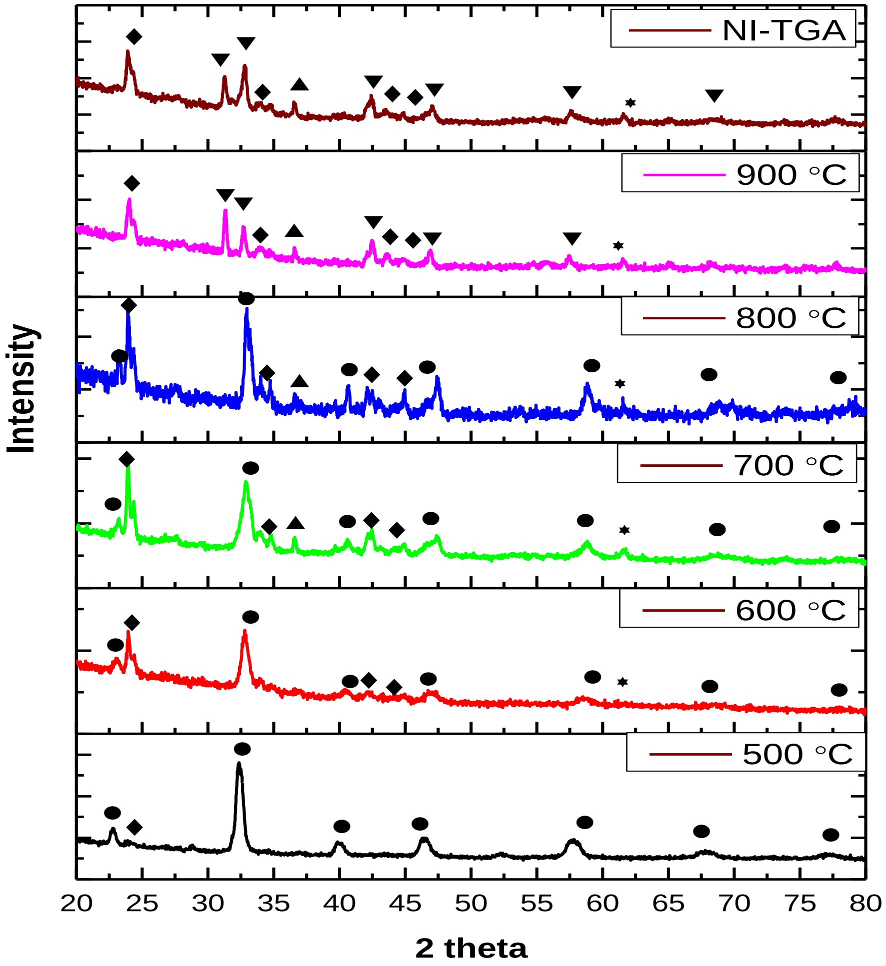

Figure 2-11 Ex-situ XRD of carbonated LBC in 100 % CO_2 (phases are ●- LBC/$LaCoO_3$ ♦-$BaCO_3$ (ortho) ▲-CoO ▼- $LaCoO_4$)

In addition to isothermal TGA, LBC-CO_2 reaction was investigated using in-situ X-ray diffraction studies. In order to capture phase transformation kinetics during carbonation, a scanning interval of 20 minutes was chosen and isothermal time dependent HT -XRD were measured at 600 ºC and 800 ºC. The results are presented in Figure 2-12 and 2-13.

Figure 2-12 shows reaction progress monitored by in-situ XRD at 600ºC. Only two major phases – LBC and $BaCO_3$-could be identified throughout the 180 minutes of reaction monitored. The barium carbonates exist in the orthorhombic form. The raw peak intensity of orthorhombic barium carbonate (at $2\theta = 23.8$) phase gradually increases with time. A plot of $BaCO_3$ peak intensity as a function of reaction time is presented in Figure 2-14 and shows a slow increase in the intensity consistent with a slow reaction of LBC observed in TGA measurements (Figure 2-10). The overall reaction describing this process is reaction (2-2). The presence of CoO was expected in the XRD data with peak at $2\theta \approx 36.5$. Further, CoO and $BaCO_3$ should exist in equimolar amounts as per the stoichiometry of reaction (2-2). The only reason CoO is not observed can be attributed to lower intrinsic intensity of CoO compared to that for $BaCO_3$. The presence of CoO in the in-situ XRD at 800 °C was noted as shown in Figure 2-13. The rhombohedra barium carbonate phase was observed and quantification of its peak intensity as a function of time as shown in Figure 2-13 indicates that no changes in $BaCO_3$ peak intensity occurs after 20 minutes of reaction. That is, the conversion of LBC is completed within the first 20 minutes. This is consistent with the TGA measurements at 800°C.

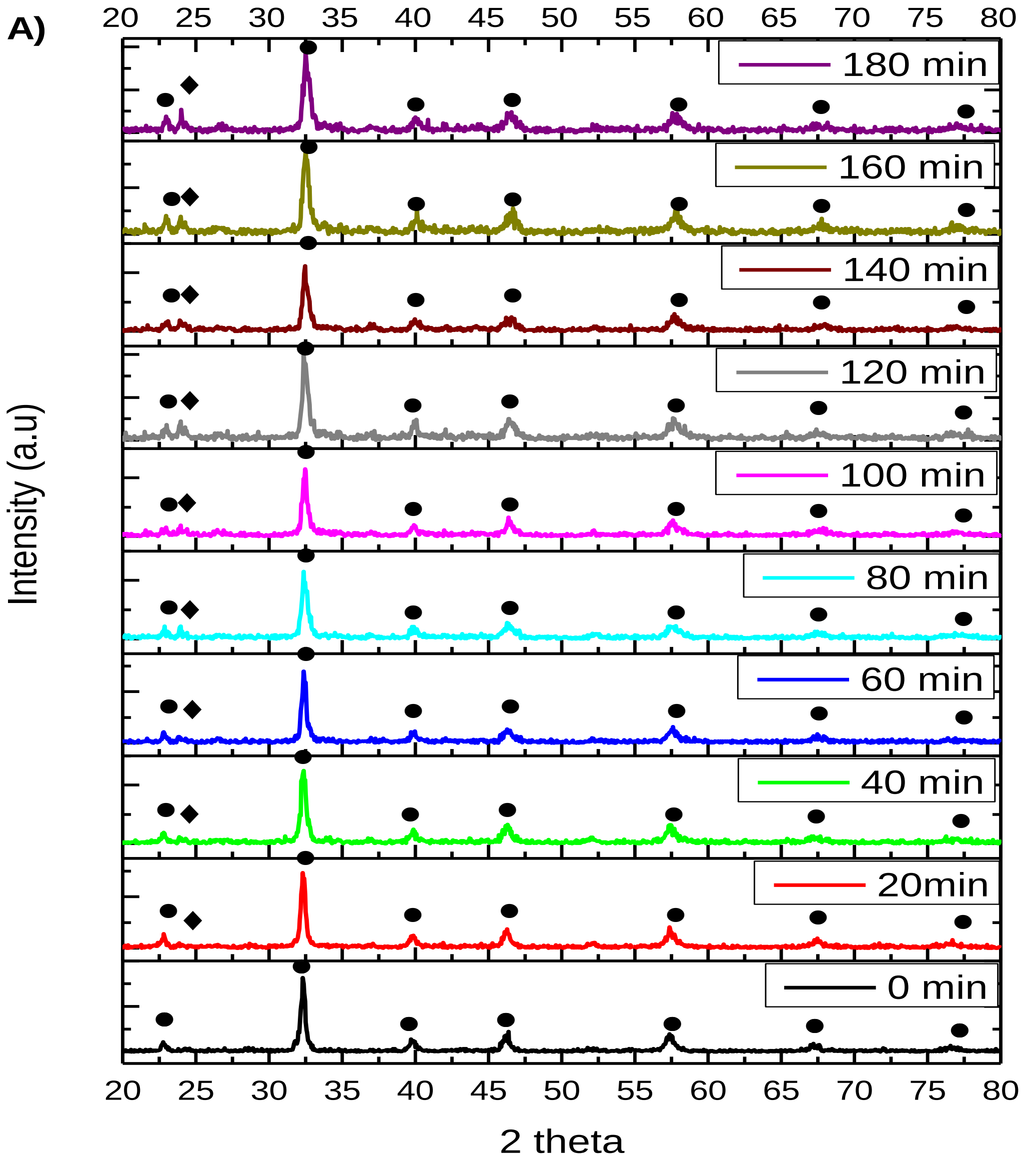

Figure 2-12 Isothermal HT-XRD studies in 100% carbon dioxide atmosphere at 600 °C(A) ((●- LBC/$LaCoO_3$; ♦- $BaCO_3$ (ortho);Δ-$BaCO_3$ (rhombo) ; ▼ - CoO)

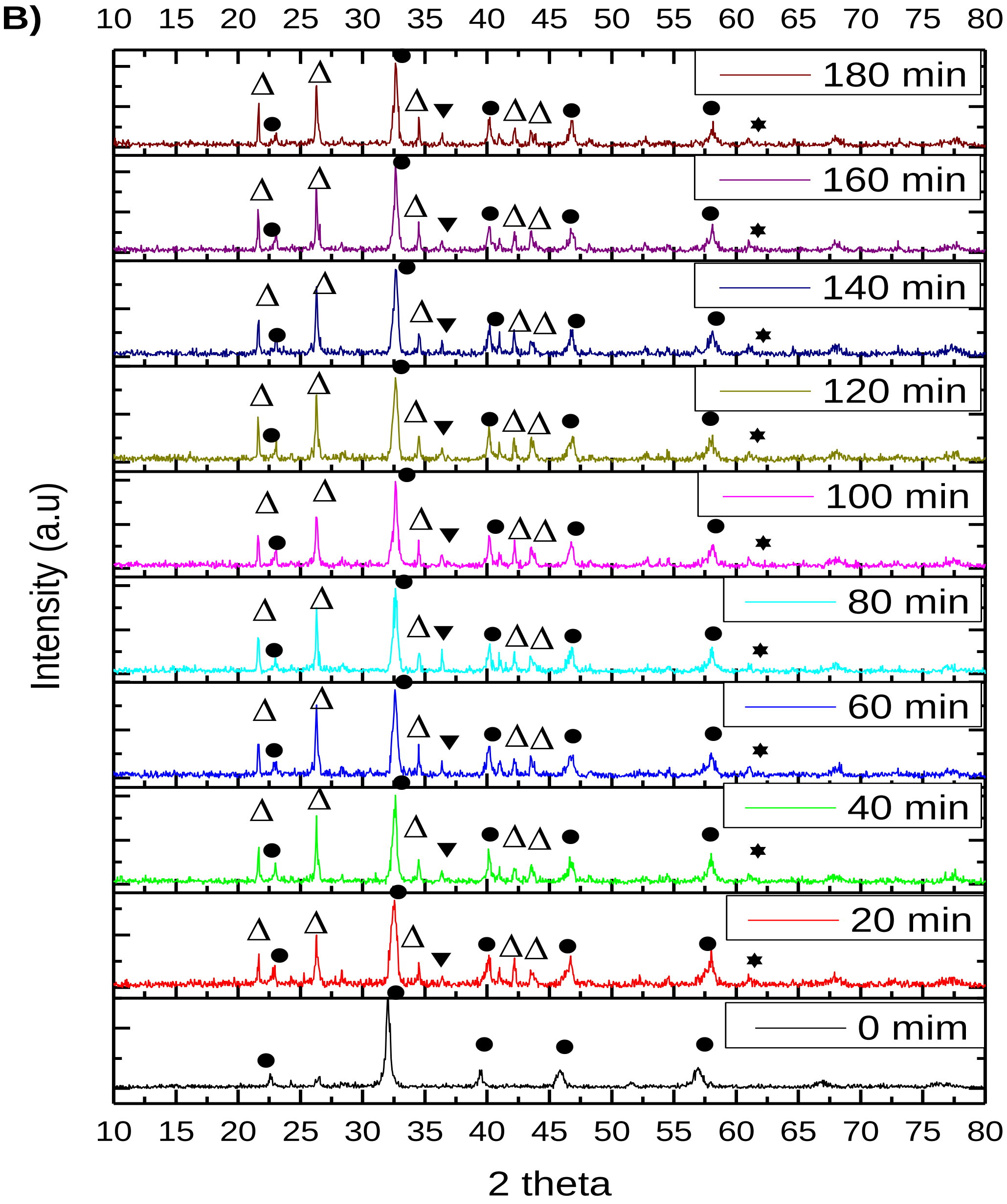

Figure 2-13 Isothermal HT-XRD studies in 100% carbon dioxide atmosphere at 800 °C ((●- LBC/$LaCoO_3$; ♦- $BaCO_3$ (ortho);Δ-$BaCO_3$ (rhombo) ; ▼ - CoO))

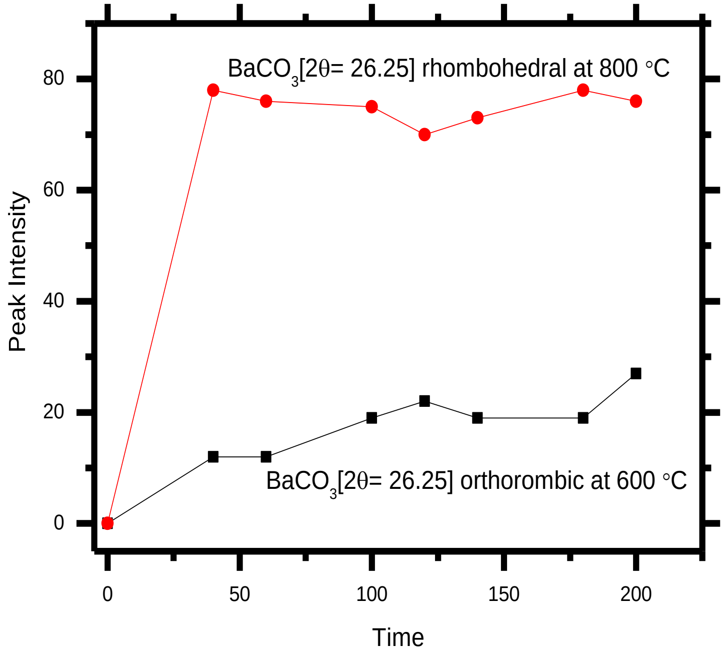

Figure 2-14 Raw peak intensity of $BaCO_{3\ (ortho)}$ and $BaCO_{3\ (rhombo)}$ at 600 °C and 800 °C, respectively.

2.3.1.3 Carbonation Kinetics

An analysis of the kinetics of the carbonation reaction data presented in Figure 2-10 was carried out. A number of different kinetics models have been proposed for the carbonation of alkali based metal oxides such as homogeneous [28], shrinking core [28], double shell [29] and double exponential [30] to understand the nature of the reaction and to extract reaction kinetics parameters. Here, a simple homogenous model, similar to that proposed by Lin et al. [28], was adopted to fit the TGA data.

The model equation (see appendix A for model derivation and assumption) for the proposed kinetics,

$$X_A = 1 - \frac{1}{1 + Kt} \tag{2-5}$$

Isothermal TGA data were regressed with the kinetic model to estimate the rate constant, K. The TGA data were expressed in terms of conversion. The time scale was scaled to zero as the time at which CO_2 was introduced into the system. Figure 2-15(a) shows a comparison of the model fit to the isothermal TGA data.

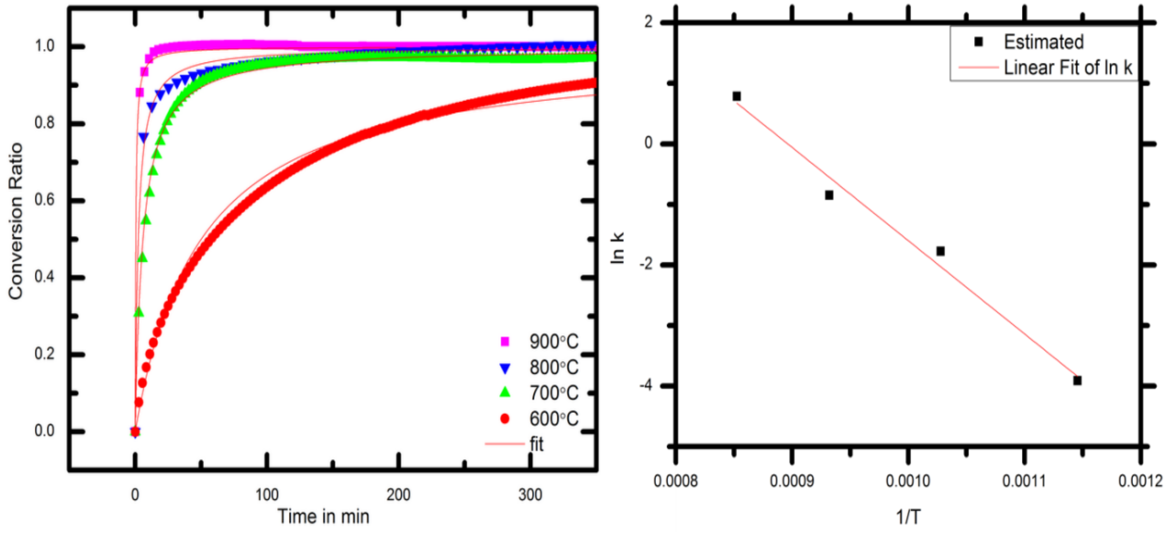

Figure 2-15 (a) Isothermal kinetics studies at 100% carbon dioxide atmosphere fitted with proposed model (b) Arrhenius plot showing dependence of reaction rate constant on temperature

The estimated rate constants are reported on an Arrhenius plot in Figure 2-15(b) and also in Table 2-1. Activation energy for the carbonation reaction of LBC under 1 atm of carbon dioxide was estimated as 128 kJ/mol.

Table 2-1 Rate constants at different temperatures

	600 °C	700 °C	800 °C	900 °C
K Value (at 1 atm of CO_2) in min^{-1}	0.02	0.17	0.43	2.1

The *in-situ* XRD data lends itself to the analysis of the carbonate kinetics as well since $BaCO_3$ peak intensity should reflect the reaction progress. Thus, carbonate conversion was calculated using peak intensity of barium carbonate using the following expression.

$$X_A = 1 - \frac{1}{1 + Kt} = 1 - \frac{I_{BaCO_3}(t)}{I_{BaCO_3}(\infty)} \tag{2-6}$$

From the Figure 2-16, it is evident that at 800 ° C, the simulated conversion curve obtained by substituting K value to the homogenous model (eqn2-5) fits well with respect to HT-XRD conversion data. However, in the case of 600°C, the simulated curve does not fit properly with the HT-XRD data. The reason for mismatch for 600°C experiment may be due to the factor that the area under the curve of XRD is more relevant in capturing kinetic information rather than the peak intensity only.

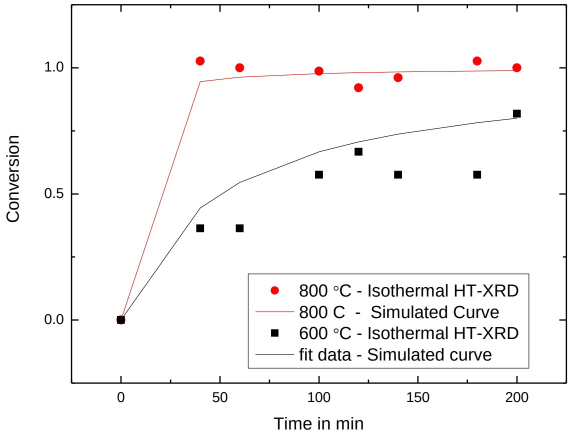

Figure 2-16 Isothermal HT peak data compared with the simulated kinetic data

2.3.1.4 Proposed overall reaction pathway

$$La_{0.5}Ba_{0.5}CoO_{3-\delta}$$

$$\text{30--500°C} \;\Big\downarrow\; \text{Oxygen non-stoichiometry}$$

$$La_{0.5}Ba_{0.5}CoO_{3-\Delta\delta} + \delta' O_2 \uparrow$$

$$\text{500°C-800°C} \;\Big\downarrow\; \tfrac{1}{2}\,CO_2 \quad \text{Carbonation reaction}$$

$$\frac{1}{2}LaCoO_3 + \frac{1}{2}BaCO_{3(ortho)} + \frac{1}{2}CoO + \frac{1-2\delta}{4}O_2 \uparrow$$

$$\text{800°C-900°C} \;\Big\downarrow\; \text{Barium carbonate phase transformation}$$

$$\frac{1}{2}LaCoO_3 + \frac{1}{2}BaCO_{3\,(rhombo)} + \frac{1}{2}CoO + \frac{1-2\delta}{4}O_2 \uparrow$$

$$\text{900°C} \;\Big\downarrow\; \text{Perovskite phase transformation}$$

$$\frac{1}{2}La_2CoO_4 + \frac{1}{2}BaCO_{3\,(rhombo)} + \frac{3}{2}CoO + \frac{1.5-2\delta}{4}O_2 \uparrow$$

Figure 2-17 Proposed LBC-CO_2 reaction pathway in pure CO_2 atmosphere

From the combined TGA, *ex-situ* XRD, and *in-situ* XRD analyses a reaction pathway shown in Figure 2-17 is proposed. The scheme did not consider decomposition of barium carbonate ($BaCO_3 \rightarrow BaO + CO_2$) as it starts around 1380 °C in 100% carbon dioxide [9].

2.3.2 Thermodynamic phase boundary for carbonate formation

Generation of the carbonate formation phase boundary for LBC will be immensely powerful tool for assessing the safe operating regime of LBC-based SOFC cathode. Moreover, the fundamental thermodynamic parameters (ΔH^o and ΔS^o) for the reaction that could be derived from the phase boundary information would be useful for other material science application. Various experimental methods such as molten salt [10], galvanic cell [10], in-situ XRD [15, 18] and TGA [11-15] have been used to determine perovskite/carbon dioxide equilibrium. In this work, TGA was employed to determine the thermodynamically relevant carbonate formation onset point. The basic idea was to heat the oxide/perovskite to sufficiently high temperature in the absence of CO_2 and then introduce the CO_2 in the system and slowly cool down such that the carbonate formation boundary was crossed and is observed as a mass increase. Such an experiment was shown in Figure 2-18 for 1 mol% CO_2 in nitrogen atmosphere. During the heating cycle in the nitrogen environment, LBC loses oxygen resulting in mass loss. Once the set-point temperature is reached, 1 mol % carbon dioxide in nitrogen was introduced, and the mixture kept isothermally for an hour and then allowed to cool down in the same atmosphere (1 mol % carbon dioxide). Upon cooling, a mass increase is observed at 850 ºC. A mass increase continued as the temperature drops to 300ºC and appears to reach a stable value. This steady-state should not be confused necessarily with completion of reaction or maximum conversion attainable. At temperatures below 850ºC carbonate formation is thermodynamically favorable but as the temperature is reduced, the kinetics of the reaction reduces dramatically such that at temperatures below 300 ºC, the reaction proceeds at negligible rate.

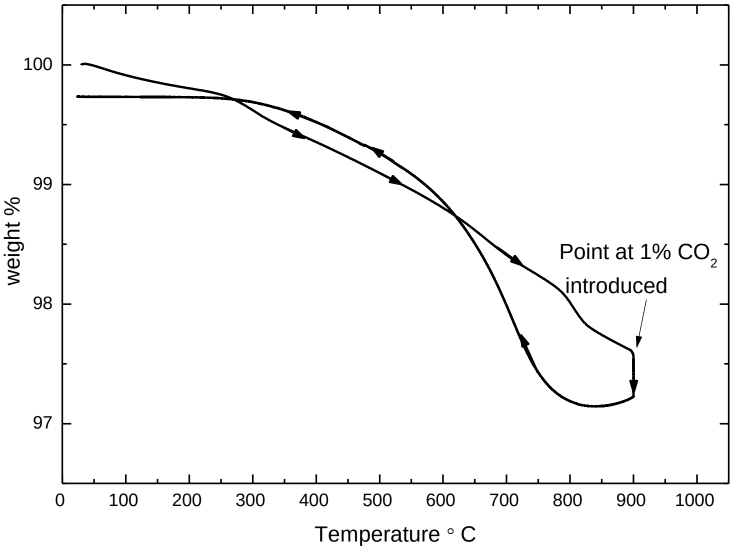

Figure 2-18 TGA of LBC during cooling experiments. LBC heated to 900 ^{o}C in nitrogen atmosphere and then CO_2-N_2 mixture containing 1 mol% CO_2 is introduced and equilibrated for an 60 minutes followed by cooling at 2^{o}C/min.

2.3.2.1 Determination of the carbonate onset temperature

The NI-TGA data for the cooling experiments (1000 °C→ 30 °C) for three different carbon dioxide partial pressure environments are presented in Fig 2-19 (a). For clarity sake, the weight at which the cooling starts was scaled as 100%.The temperature at which the weight increase was first observed was considered as the carbonate formation onset point. Ideally, to determine the thermodynamic onset temperature, the experiment needs to be done at near zero cooling rates so that the kinetic effects are eliminated. However, practically experiment at near zero cooling rates will be prohibitively time consuming. Therefore, a sufficiently low cooling rate was adopted in this study to determine the carbonate formation onset temperature. First, a high scan rate cooling experiments was carried out to narrow a temperature interval for reaction onset. Cooling TGA experiments were again done at a slower scan rate (0.3 °C/min) in that narrow temperature range. Figure 2-19 (b) shows the slow scan thermogram during cooling in a 2mol% CO_2 in N_2 environment. From the fast scan experiment, the onset temperature range of 950°C-850°C was narrowed down. It can be noted from Figure 2-19 (b) that during the initial cooling period, a mass loss due to oxygen loss continues at a seemingly constant rate and then the rate of mass loss reduced with eventual gain in mass. Arguing that the net change in mass loss rate was due to the net effect of carbonation occurring concurrently with the constant net rate of oxygen loss, the carbonate onset temperature was deemed to be the temperature at the slope of mass loss first deviates from the linear profile. This is shown in Figure 2-19 (b). Similar analysis was performed for 1% and 5% CO_2 atmosphere and p-T equilibrium was determined.

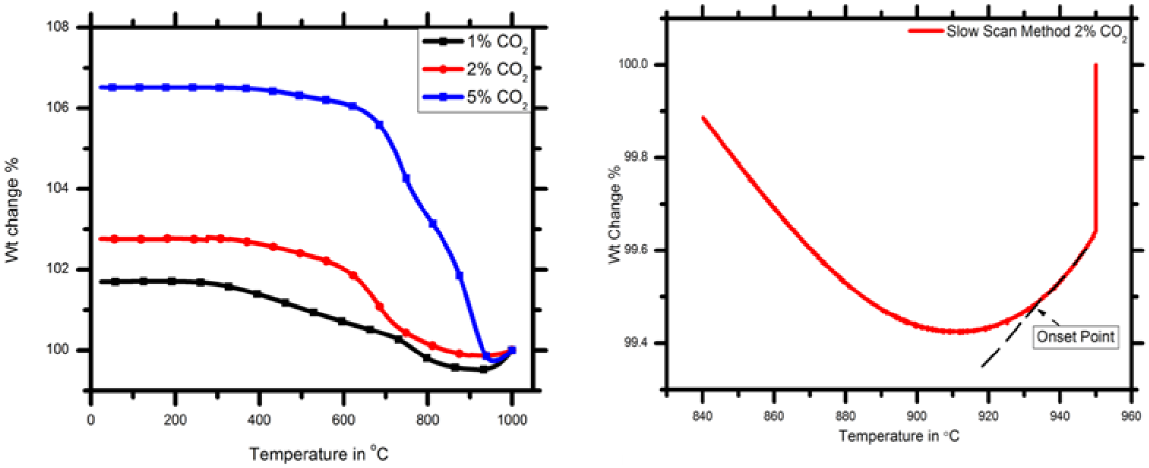

Figure 2-19 a) Carbonation reaction studies using non isothermal cooling experiment (2°C/min) under various partial pressures b) Reaction onset point determination using slow scan (cooling) experiments

2.3.2.1 Thermodynamic analysis

The carbonate formation onset temperature at different CO_2 partial pressure can be used to determine the standard state thermodynamic parameters for the reaction. For the analysis, the following overall equilibrium LBC carbonation reaction was considered:

$$2\,La_{0.5}Ba_{0.5}CoO_{3-\delta} + CO_2 \overset{K_p}{\leftrightarrow} BaCO_3 + CoO + LaCoO_3 + \frac{1-2\delta}{2}O_2\uparrow \tag{2-7}$$

Here, formation of La_2CoO_4 phase was not considered as it may forms only at high carbon dioxide partial pressure. In addition, as will become apparent that the analysis does not necessarily require a complete knowledge of what products are formed. The reaction Gibbs energy $\Delta_r G$ of above reaction (2-7) can be written as:

$$\Delta_r G(T) = \Delta_r G°(T) + RT \ln Q \qquad 2\text{-}8$$

where, $\Delta_r G^o$ standard Gibbs energy of reaction, R is gas constant and T is temperature.

The reaction quotient, Q has the form

$$Q = \frac{\prod(activity\ of\ product)}{\prod(activity\ of\ reactant)} = \frac{a_{BaCO_3} \times a_{CoO} \times a_{LaCO_3} \times a_{O_2}^{\frac{1-2\delta}{2}}}{a^2_{La_{0.5}Ba_{0.5}CoO_{3-\delta}} \times a_{CO_2}} \qquad 2\text{-}9$$

Considering that the activity (a) of pure solid such as $BaCO_3$, CoO, $LaCoO_3$, $La_{0.5}Ba_{0.5}CoO_{3-\delta}$ as unity and the activity of gaseous species as: $a_{CO_2} = \frac{P_{CO_2}}{P_o}$ $a_{O_2} = \frac{P_{O_2}}{P_o}$

the eqn. 2- 8 reduces to the following expression:

$$\Delta_r G(T) = G°(T) - RT \ln P_{CO_2} + \frac{1-2\delta}{2} RT \ln P_{O_2} \qquad 2\text{-}10$$

It is useful to mention that since the activity of solid phase is considered to be one, whether the reaction product is considered to contain $LaCoO_3$ or La_2CoO_4 does not affect the free energy calculation. At equilibrium, $\Delta_r G = 0$, so the eqn. 2-10 can be written as:

$$\Delta_r G°(T) = RT \ln P_{CO_2} - \frac{1-2\delta}{2} RT \ln P_{O_2} \qquad 2\text{-}11$$

Substituting $\Delta_r G^\circ = \Delta_r H^o - T\Delta_r S^o$ and

$$ln\,P_{CO_2} = \frac{\Delta_r H°}{RT} - \frac{\Delta_r S°}{R} + \frac{1-2\delta}{2} lnP_{O_2} \qquad \text{2-12}$$

In equation 2-12, the P_{CO2} corresponds to the partial pressure at which the onset temperature (T) was determined.

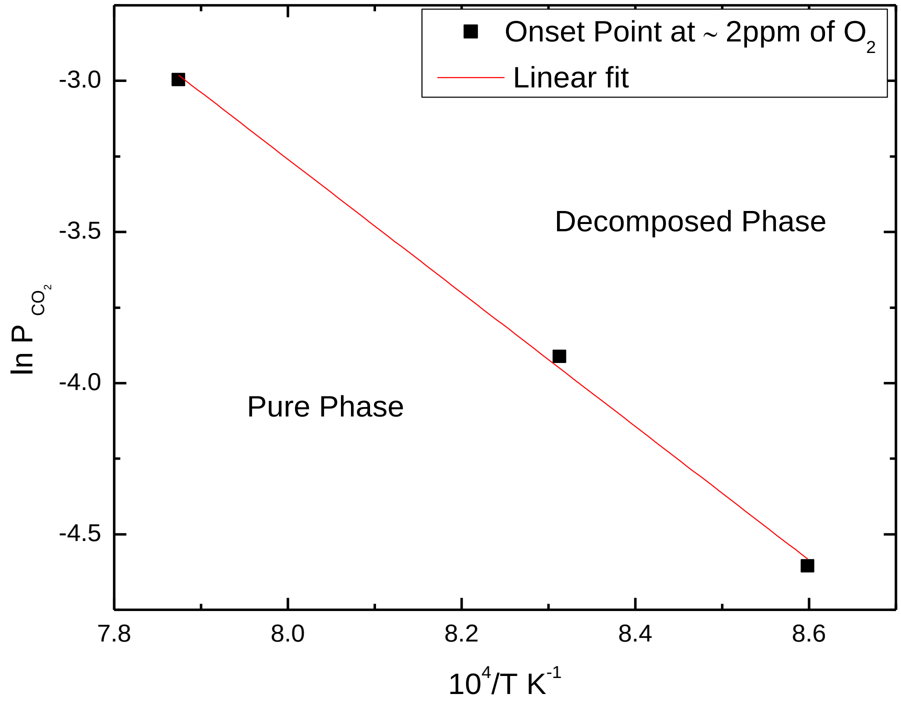

Figure 2-20 Phase stability of LBC in carbon dioxide atmosphere

From equation (2-12), it is apparent that an Arrhenius plot of $\ln P_{CO_2}$ versus onset temperature yields a slope equal to (Δ_rH°/R) and an intercept equal to $-\frac{\Delta_r S°}{R} + \frac{1-2\delta}{2} lnP_{O_2}$.

The Arrhenius plot of $\ln P_{CO_2}$ and temperature is shown in Figure 2-20. From the slope of the plot, the $\Delta_r H°$ was determined to be -184 KJ/mol.

To estimate the standard state entropy of the reaction, considerations of oxygen content in the CO_2 stream and oxygen non-stoichiometry (δ) had to be made. The experiments in this study were done in CO_2/N_2 mixture and the supply gas contains 2 ppm level of oxygen [32].

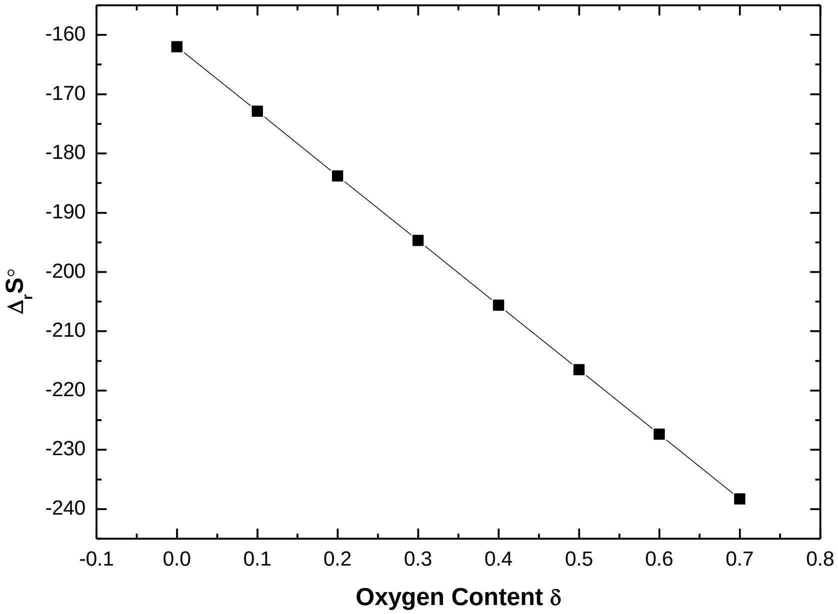

Figure 2-21 Variation of $\Delta_r S°$ with respect to oxygen content

On the other hand, oxygen non-stoichiometry (δ) is function of oxygen partial pressure, temperature and varies between 0 and 0.7 at higher temperature [13]. Therefore $\Delta_r S°$ was determined for a range of δ valueas shown in Figure 2-21. In the δ range of 0 to 0.7, the

$\Delta_r S°$ value varies between -160 J/mol.Kand -240 J/mol.K, respectively. This compares well with the value reported barium-based-perovskite-CO_2 reaction equilibrium in the literature [11, 15].

2.3.3 Prediction of carbonate formation phase boundary at SOFC operation condition

The thermodynamic parameters for the reaction are a powerful tool in predicting the carbonate formation phase boundary of LBC for various applications. The application of interest in this thesis is solid oxide fuel cells wherein LBC can be used as the material for cathode. Using the $\Delta_r H°$ and $\Delta_r S°$ determined above, the onset temperature corresponding to CO_2 in ambient air of 380 ppm was computed by considering oxygen partial pressure as 0.21 atm and a δ value of 0.25. Here $\Delta_r S°$ was considered as 240J/mol.K. The phase boundary generated from these calculations is reported in Figure 2-22. From the figure it can be noted that to avoid carbonate formation on LBC cathode of a SOFC fed with ambient air (0.21 atm of O_2 and 380 ppm of CO_2), it should be operated above 610°C.

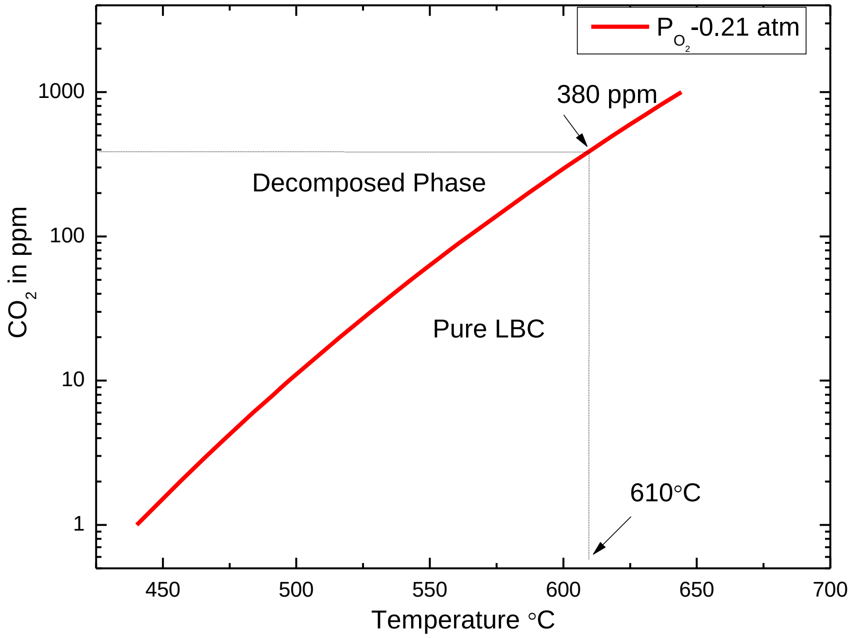

Figure 2-22 Prediction carbonate formation phase boundary at ambient air condition

2.4 Summary

In the present work, we examined the LBC – CO_2 reaction in detail and established a phase boundary between LBC and decomposed phase. Two techniques, namely TGA along with in-situ HT-XRD, were used to investigate LBC decomposition reaction and its pathway in the range of 30°C -900 °C. In addition, a homogenous kinetic model was used to extract reaction rate parameters.

Secondly, TGA cooling experiments in different carbon dioxide partial pressure was done to determine phase boundary between pure LBC and decomposed phase. Subsequently, the obtained thermodynamic parameters obtained was extended to determine equilibrium reaction temperature in air (i.e 0.03% CO_2) and predicted that LBC based SOFC when fed with air should be operated above 610 °C in order to completely neglect carbonate formation or LBC decomposition.

2.5 Reference

1) Will, J.; Mitterdorfer, A.; Kleinlogel, C.; Perednis, D.; Gauckler, L. J. Fabrication of Thin Electrolytes for Second-Generation Solid Oxide Fuel Cells. *Solid State Ionics* **2000**, *131*, 79-96.
2) Wachsman, E. D.; Lee, K. T. Lowering the Temperature of Solid Oxide Fuel Cells. *Science* **2011**, *334*, 935-939.
3) Wachsman, E. D.; Singhal, S. C. Solid Oxide Fuel Cell Commercialization, Research and Challenges. *American Ceramic Society Bulletin* **2010**, *89*, 22-32.
4) Shao, Z. P.; Haile, S. M. A High-Performance Cathode for the Next Generation of Solid-Oxide Fuel Cells. *Nature* **2004**, *431*, 170-173.
5) Zhou, W.; Ran, R.; Shao, Z. Progress in Understanding and Development of $Ba_{0.5}Sr_{0.5}Co_{0.8}Fe_{0.2}O_{3-delta}$-Based Cathodes for Intermediate-Temperature Solid-Oxide Fuel Cells: A Review. *J. Power Sources* **2009**, *192*, 231-246.

6) Amin, R.; Karan, K. Characterization of $La_{0.5}Ba_{0.5}CoO_{3-delta}$ as a SOFC Cathode Material. *J. Electrochem. Soc.* **2010**, *157*, B285-B291.

7) Amin, R.; Kenney, B.; Karan, K. Characterizations of LBC-GDC Composite Cathodes for Low Temperature SOFCs. *J. Electrochem. Soc.* **2011**, *158*, B1076-B1082.

8) Ryu, K. H.; Haile, S. M. Chemical Stability and Proton Conductivity of Doped $BaCeO_3$-$BaZrO_3$ Solid Solutions. *Solid State Ionics* **1999**, *125*, 355-367.

9) Scholten, M. J.; Schoonman, J.; Vanmiltenburg, J. C.; Oonk, H. A. J. Synthesis of Strontium and Barium Cerate and their Reaction with Carbon-Dioxide. *Solid State Ionics* **1993**, *61*, 83-91.

10) Gopalan, S.; Virkar, A. V. Thermodynamic Stabilities of $SrCeO_3$ and $BaCeO_3$ using a Molten-Salt Method and Galvanic Cells. *J. Electrochem. Soc.* **1993**, *140*, 1060-1065.

11) Zakowsky, N.; Williamson, S.; Irvine, J. T. Elaboration of CO2 Tolerance Limits of $BaCe_{0.9}Y_{0.1}O_3$ Electrolytes for Fuel Cells and Other Applications. *Solid State Ionics* **2005**, *176*, 3019-3026.

12) Yang, Z.; Harvey, A. S.; Gauckler, L. J. Influence of CO_2 on $Ba_{0.2}Sr_{0.8}Co_{0.8}Fe_{0.2}O_{3-delta}$ at Elevated Temperatures. *Scr. Mater.***2009**, *61*, 1083-1086.

13) Fjellvag, H.; Karen, P.; Kjekshus, A.; Kofstad, P.;Norby, T. Carbonatization of $YBa_2Cu_3O_{6+x}$. *ActaChemicaScandinavica Series A-Physical and Inorganic Chemistry* **1988**, *42*, 178-184.

14) Degterov, S. A.; Voronin, G. F. Effects of CO_2 on Thermodynamic Stability of Superconductors in the Y-Ba-Cu-O System. *Physica C: Superconductivity* **1993**, *208*, 403-411.

15) Kohav, T.; Forster, K. M.; Richardson, J. T.; Luss, D. Effect of Ambient and Evolved CO_2 on an Equilibrium Reaction in $YBa_2Cu_3O_{6+X}$ Synthesis. *Mater. Res. Bull.* **1996**, *31*, 1111-1119.

16) Bhella, S. S.; Shafi, S. P.; Trobec, F.; Bieringer, M.; Thangadurai, V. In-Situ Powder X-Ray Diffraction Investigation of Reaction Pathways for the $BaCO_3$-CeO_2-In_2O_3 and CeO_2-In_2O_3 Systems. *Inorg. Chem.* **2010**, *49*, 1699-1704.

17) Efimov, K.; Czuprat, O.; Feldhoff, A. In-Situ X-Ray Diffraction Study of Carbonate Formation and Decomposition in Perovskite-Type BCFZ. *Journal of Solid State Chemistry* **2011**, *184*, 1085-1089.

18) Besmann, T.M. and Carneim, R.D. and Armstrong, T.R In *Decomposition of Yttrium-Doped Barium Cerate in Carbon Dioxide;* Inorganic membranes for energy and environmental applications; Springer Verlag(Berlin, Germany)2008; pp 83.

19) Yan, A.; Cheng, M.; Dong, Y. L.; Yang, W. S.; Maragou, V.; Song, S. Q.; Tsiakaras, P. Investigation of a $Ba_{0.5}Sr_{0.5}Co_{0.8}Fe_{0.2}O_{3-delta}$ Based Cathode IT-

SOFC - I. the Effect of CO2 on the Cell Performance. *Applied Catalysis B-Environmental* **2006**, *66*, 64-71.

20) Yan, A.; Yang, M.; Hou, Z.; Dong, Y.; Cheng, M. Investigation of $Ba_{1-x}Sr_xCo_{0.8}Fe_{0.2}O_{3-delta}$ as Cathodes for Low-Temperature Solid Oxide Fuel Cells both in the Absence and Presence of CO_2. *J. Power Sources* **2008**, *185*, 76-84.

21) Mizusaki, J.; Mima, Y.; Yamauchi, S.; Fueki, K.; Tagawa, H. Non-stoichiometry of the Perovskite-Type Oxides $La_{1-X}Sr_xCoO_{3-delta}$. *Journal of Solid State Chemistry* **1989**, *80*, 102-111.

22) Opila, E. J.; Tuller, H. L. Thermogravimetric Analysis and Defect Models of the Oxygen Non-stoichiometry in $La_{2-X}Sr_xCuO_{4-Y}$. *J Am Ceram Soc***1994**, *77*, 2727-2737.

23) Liu, L.; Lee, T.; Qiu, L.; Yang, Y.; Jacobson, A. A Thermogravimetric Study of the Phase Diagram of Strontium Cobalt Iron Oxide, $SrCo_{0.8}Fe_{0.2}O_{3-delta}$. *Mater. Res. Bull.* **1996**, *31*, 29-35.

24) Karppinen, M.; Niinistö, L.; Yamauchi, H. Studies on the Oxygen Stoichiometry in Superconducting Cuprates by Thermoanalytical Methods. *Journal of Thermal Analysis and Calorimetry***1997**, *48*, 1123-1141.

25) Palcut, M.; Wiik, K.; Grande, T. Cation Self-Diffusion in $LaCoO_3$ and La_2CoO_4 Studied by Diffusion Couple Experiments. *The Journal of Physical Chemistry B* **2007**, *111*, 2299-2308.

26) Radovic, M.; Speakman, S. A.; Allard, L. F.; Payzant, E. A.; Lara-Curzio, E.; Kriven, W. M.; Lloyd, J.; Fegely, L.; Orlovskaya, N. Thermal, Mechanical and Phase Stability of $LaCoO_3$ in Reducing and Oxidizing Environments. *J. Power Sources* **2008**, *184*, 77-83.

27) Petrov, A. N.; Cherepanov, V. A.; Kononchuk, O. F.; Gavrilova, L. Y. Oxygen Nonstoichiometry of $La_{1-x}Sr_xCoO_{3-\delta}$ $(0 < x \leq 0.6)$. *Journal of Solid State Chemistry* **1990**, *87*, 69-76.

28) Yang, Q.; Lin, Y. Kinetics of Carbon Dioxide Sorption on Perovskite-Type Metal Oxides. *Ind. Eng. Chem. Res.***2006**, *45,* 6302-6310.

29) Xiong, R.; Ida, J.; Lin, Y. Kinetics of Carbon Dioxide Sorption on Potassium-Doped Lithium Zirconate. *Chemical engineering science* **2003**, *58,* 4377-4385.

30) Venegas, M. J.; Fregoso-Israel, E.; Escamilla, R.; Pfeiffer, H. Kinetic and Reaction Mechanism of CO_2 Sorption on Li_4SiO_4: Study of the Particle Size Effect. *Ind. Eng. Chem. Res.***2007**, *46*, 2407-2412.

31) Troyanchuk, I.; Kasper, N.; Khalyavin, D.; Chobot, A.; Chobot, G.; Szymczak, H. Magnetic and Structural Phase Transitions in some Orthocobaltites Doped by Ba Or Sr Ions. *Journal of Physics: Condensed Matter* **1998**, *10,* 6381.

32) Private Communications (January 12, 2012) with Sales Representative of Praxair Gas Supplies, Kingston.

33) Selvaduray, G.; Zhang, C.; Balachandran, U.; Gao, Y.; Merkle, K.; Shi, H.; Poeppel, R. Effect of CO_2 on the Processing of Y–Ba–Cu–O Superconductors. *J. Mater. Res.* **1992**, *7*, 283-291.

34) El-Shinawi, H. Z. I. Synthesis and Characterization of Cobalt-Containing Perovskite-Type Oxides. PhD thesis, *University of Birmingham***,** 2010**.**

Chapter 3

Development of test system for rapid testing of multiple electrodes of reproducible features

3.1 Introduction

Development of new electrode materials can be expedited significantly, by combining a fabrication method that can be used to make reproducible electrodes and a testing method that can examine several electrodes in a short period of time [1-7]. The latter also helps to generate performance data that is statistically significant.

In case of SOFCs, fabrication of electrodes in academic research facilities often involves manual or semi-automatic process. For example, the electrodes are fabricated by using hand-held spray guns and hand painting of electrode ink on an appropriate substrate (electrolyte). Reproducibility of electrodes made by such processes can be a significant problem. In contrast, automated systems such as inkjet printing technique offers the advantages of drop-on-demand printing and designs with controlled, reproducible features [7-11]. Furthermore, inkjet printing systems have relatively fine resolution control such that features of 20-30 μm can be printed [12-13]. The thickness of the printed structure can be varied and controlled by layer-by-layer printing offering another advantage. Thus, inkjet printing offers the possibility of fabricating multiple electrodes of controlled features (thickness, size) on relatively small substrate [14-15].

Millimeter or micron-sized electrodes can be examined using micro-contact impedance spectroscopy (MCIS) [16-22]. Since multiple electrodes can be deposited on single test sample, rapid testing is possible by simply changing the electrical contact from one electrode to another without the time required to assemble and disassemble the setup and time required to heat and cool the test stage. Thus, MCIS of multiple electrodes on a single sample permits rapid generation of large data set, and, thereby, allowing statistically significant information on the performance characteristics of the sample.

The aims of this work were: to study the feasibility of fabricating miniature or micro electrodes of reproducible geometry using an existing (but new) Materials Printer, to develop the test system and establish a test protocol for testing small sized electrodes, and to gather electrode-to-electrode variability information for Ag electrodes.

3.2 Experimental section

3.2.1 Materials

Commercially available silver conductive ink (CCI-300, Cabot printed electronics, Boston, USA) was used as ink for electrode deposition. Fluid physical properties of the ink are summarized in Table 3-1.

Table 3-1 Properties of Silver Ink

Properties	**Range Value**
Viscosity at 22 ^{o}C(cP)	11-15
Surface tension at 25^{o}C(nN/m)	30-33
Silver solid loading (wt %)	19-21
Vehicle	Alcohol based

A dense single crystal of 8 mol% yttria-stabilized zirconia (MTI Corporation, USA) was used as the electrolyte, i.e. the substrate upon which the Ag electrodes were deposited. Physical properties of the 8 mol% yttria-stabilized zirconia (YSZ) are summarized in Table 3-2.

Table 3-2 Properties of YSZ single crystal

Properties	**Range Value**
Geometry	10 mm x 10 mm x 0.5mm ±0.05 mm
Orientation	(100) ± 0.5 Deg
Surface roughness	< 5 Å
Crystal Growth Technique	Flux Technique

Silver paste (SPI conductive silver paste plus^{TM}, USA) was used as counter electrode and 0.5mm thick high resistive undoped silica wafer (MTI Corporation, USA) was used as substrate.

3.2.2 Inkjet Printing

Silver micro-electrodes on yttria -stabilized zirconia (YSZ) electrolyte were deposited using Dimatix Materials Printer DMP-2800, which is based on a piezoelectric drop-on-demand inkjet technology. 1.5 ml of silver conductive ink was filled in printer cartridge, which has 16 nozzles linearly spaced at 254 microns. The printer was set to deposit five layer of given input design, as shown in Figure 3-1, on commercial YSZ single crystal (MTI Corporation). There are several settings on the printer that may need to be optimized for each application. In this case, after several trails, a printing head setting with 10 µm drop spacing, 32 V firing volts and 12Hz tickle frequency were found to be adequate. After printing and drying in air, the electrodes were cured at 200 °C for an hour. A slow ramp rate of 0.5 °C/min was used during the curing step to reduce coffee ring effect [23-24], discussed in section 3.3.1.

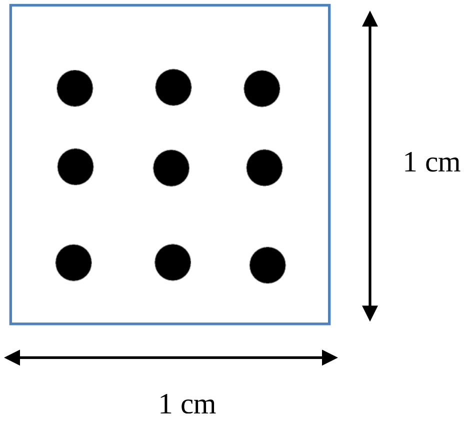

Figure 3-1 Input design for printing microelectrode in inkjet printer

3.2.3 Preparation of test cell for electrochemical testing of printed electrodes

The fabrication method described in the previous section yields multiple working electrodes (Ag electrodes) on an electrolyte (YSZ substrate). For electrochemical testing, counter electrode is required to complete the circuit. Counter electrodes were fabricated by applying silver paste (SPI conductive silver paste plus^{TM}, West Chester, USA) to the backside of the microelectrode printed YSZ single crystal.

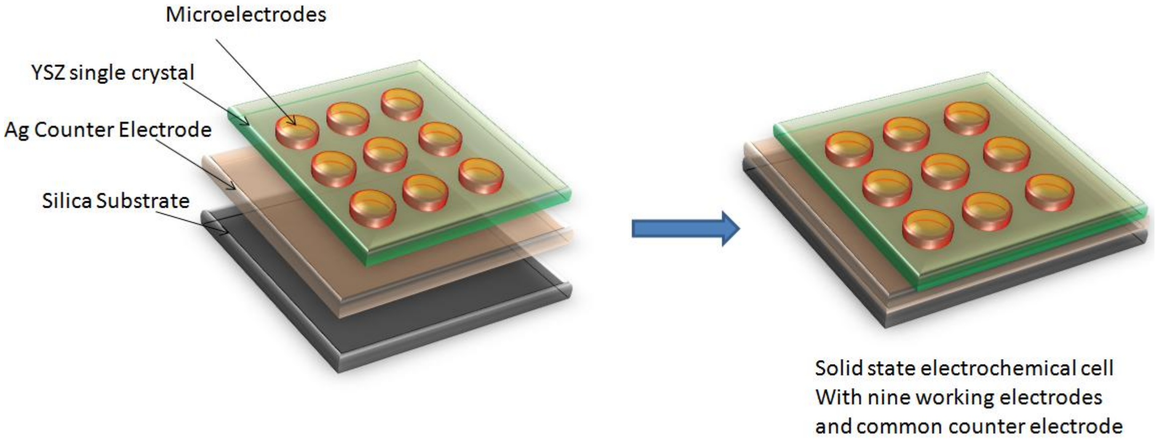

Figure 3-2 Discription of electrochemcial cell with nine identical working electrode,YSZ electrolyte, common counter electrode and silica substrate.

The counter electrode is several times larger than the working electrode so as to generate low counter electrode impedance. The sample was attached to silica wafer (MTI Corporation, Richmond, USA) to ensure good thermal contact with the heating stage below. Thus, a system of nine identical solid-state electrochemical cells (Ag microelectrode (working electrode)/YSZ (electrolyte)/porous Ag layer (counter electrode)) with common counter electrode was fabricated to study ORR kinetics as shown in Figure 3-2.

3.2.4 Physical and Electrochemical Characterization

Optical gaging product (OGP Avant ZIP 400 Video Measuring System, Rochester, NY USA) equipped with MeasureMind 3D® MultiSensor metrology software, was used to characterize full 3D and surface profile of deposited electrode. Truemap® software was used to analyze and compute geometry from the obtained OGP data.

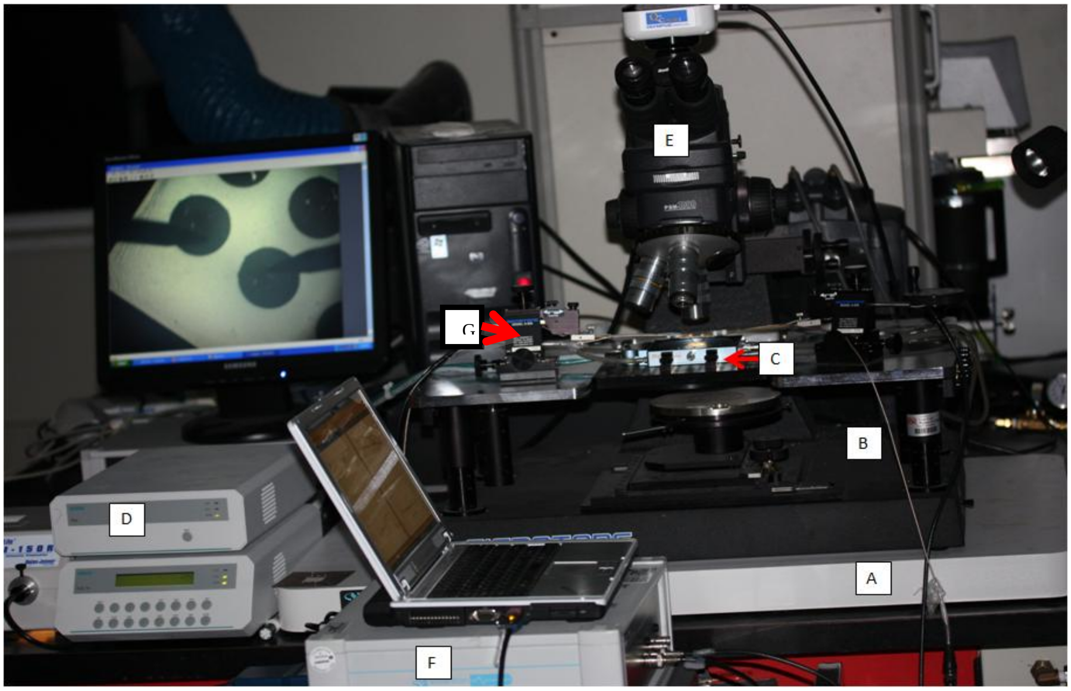

Figure 3-3 Photograph showing the micro-contact impedance spectroscopy (MCIS) setup (A) vibration isolation table(Newport Benchtop^{TM}) , (B) microprobe station

(Signatone1160), (C) furnace chamber (Linkam), (D) temperature controller, (E) optical microscope (Olymbus America Inc), (F) Electrochemical interface (solartron 1296), (G) micromanipulators (signotone model 8-926)]

An electrochemical study for the fabricated solid-state electrochemical cell was carried out using micro-contact impedance spectroscopy (MCIS). The MCIS setup (Figure 3-3) consists of vibration isolation table (Newport Benchtop^{TM}, France) over which microprobe station (S-1160 Probe Station, SignatoneCorporation, US) equipped with the hot stage (TS1000, Linkam Scientific Instruments, UK) temperature controlled stage (Linkam Scientific Instruments, UK),cooling chamber (Eheim GmbH, Germany) and optical microscope (Olympus America Inc, US) were placed.

The working and counter electrodes were electrically contacted with platinum-coated tungsten carbide needles as depicted in Figure 3-4. Micromanipulators (model 8-926, Signatone Corporation, US) were used to position needle on the electrode. Electrochemical impedance spectroscopy (EIS) was measured using dielectric interface (model 1296, Solartron,UK) connected to frequency response analyzer (model SI 1260, Solatron, UK) and data were collected in the frequency range of 10^{7} to 10^{-2} Hz.

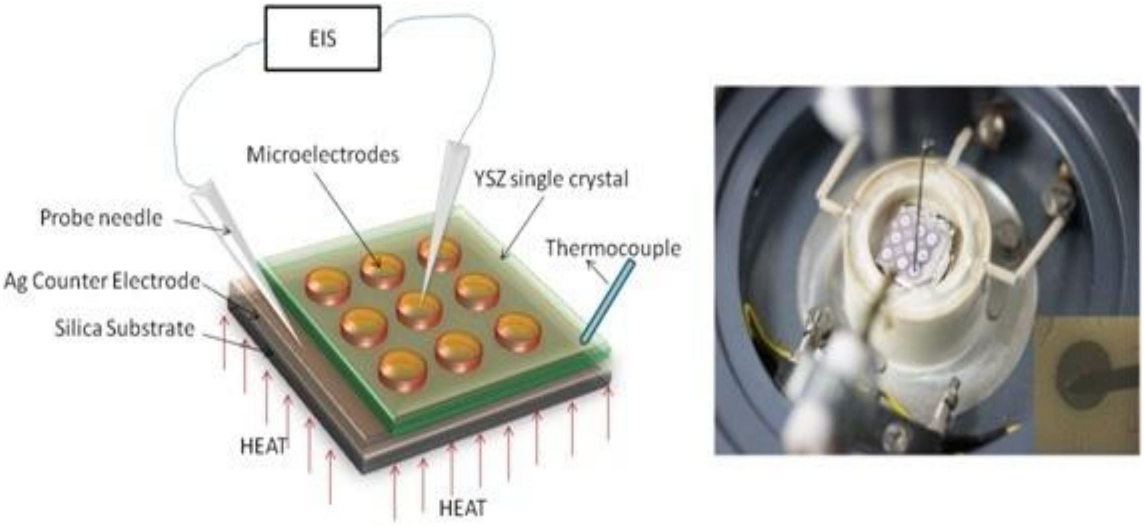

Figure 3-4 A) Schematic experimental setup for measuring impedance at Ag microelectrodes using micro-contact impedance spectroscopy. B) Photograph showing hot stage with electrochemical cell [inset image taken by optical microscope showing Pt coated tungsten carbide needle electrical contact with the microelectrode]

EIS were measure in the temperature range of 450°C -550°C under ambient air atmosphere. Temperature range of 450 -550 °C was chosen because below 450 °C the effect of YSZ grain and grain boundary appears in the impedance response, whereas above 550 °C silver evaporation can occur. Temperature of the electrode was measured by contacting a thin thermocouple (K-type, 0.5 mm probe diameter, OMEGA, Laval, Canada).

3.3 Results and discussion

3.3.1 Electrode geometry and surface profile

The electrode geometry and surface profile of inkjet printed Ag electrode were investigated using an imaging instrument (optical gaging product or OGP) equipped with MeasureMind 3D® MultiSensor metrology software. An image of a single electrode is shown in Fig 3-5.

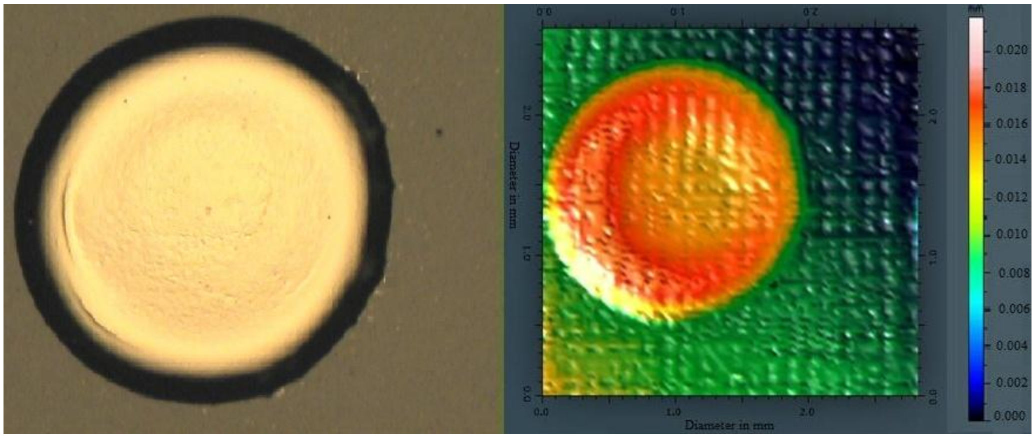

Figure 3-5 Optical image and 3D profile of one of nine electrodes deposited on YSZ electrolyte.

From the cross-sectional view shown in Figure 3-6, it was evident that the microelectrode has non-uniform thickness. The edges are higher than the inner core of the electrode. This phenomenon can be attributed to coffee ring effect during sintering [23]. Coffee ring effect occurs due to the fact that the rate of solvent evaporation is greater at the contact line and the solute segregates more around the boundary during the drying process [24].

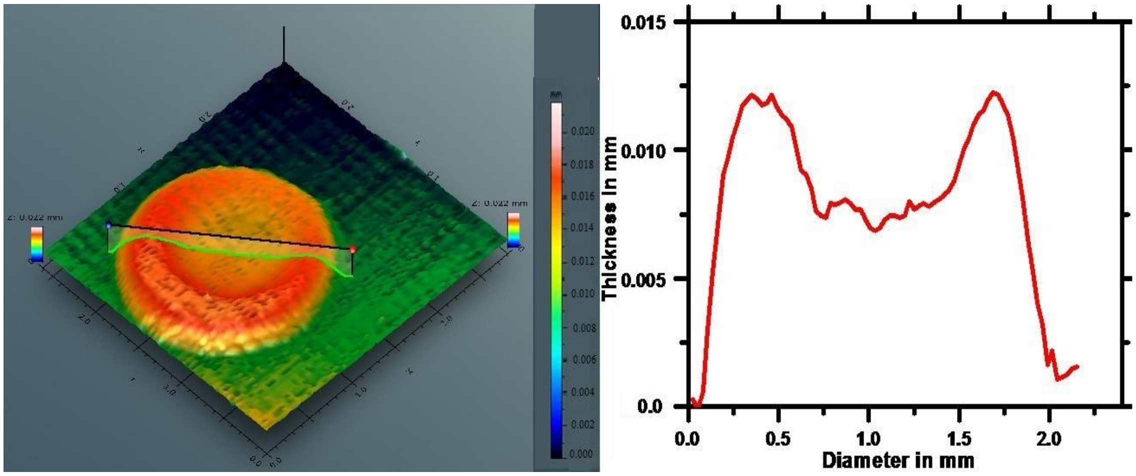

Figure 3-6 Typical surface profile of the silver electrode deposited on YSZ electrolyte [3D and 2D image].

The image analysis of the electrode allowed the determination of the electrode porosity. A porosity of 43% was estimated by applying the following equation using the measurements of the deposit weight and volume by determined from image analysis:

$$\text{Porosity}=\left(1-\frac{\text{weight of the deposit}}{\text{silver particle density x volume of the deposit}}\right)\times 100\% \qquad \text{3-1}$$

The volume of the deposit was determined using 3D profile and weight change in the substrate after the printing and heat treatment was considered as weight of the deposit.

3.3.2 Electrochemical impedance spectroscopy (EIS) of Ag microelectrodes

EIS spectra were recorded for nine identical electrodes at three different temperatures. A typical impedance response in complex-impedance-plane or Nyquist format is shown in Figure 3-7. The high frequency intercepts with real axis corresponds to pure Ohmic resistance (R_s) and difference between the low and high frequency intercept is due to electrode polarization resistance (R_p). Here, R_p represents the net effect of polarization arising from mass transport, adsorption/desorption and electrochemical kinetics for oxygen reduction reaction at Ag/YSZ interface. That is, the mechanism of ORR at cathode/electrolyte interface is a multistep processes and usually includes several parallel and series reaction pathways [28-33].

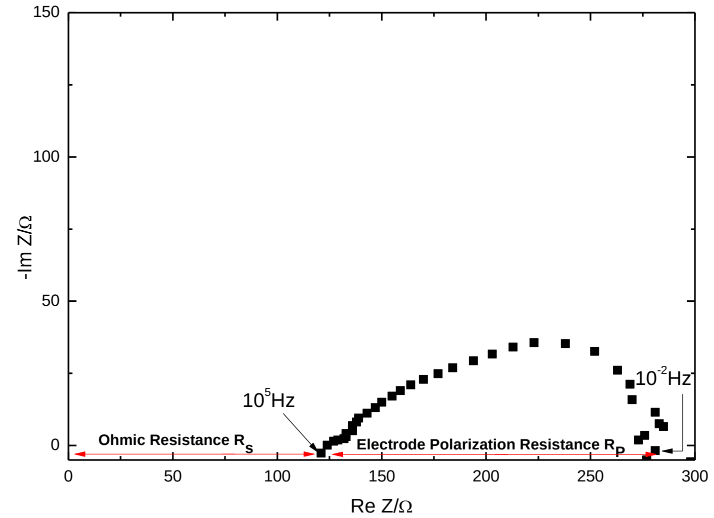

Figure 3-7 Impedance spectroscopy of a micro Ag/YSZ/Ag cell measured at 500 °C in air atmosphere

3.3.3 Validating electrochemical cell design

3.3.3.1 Effect of counter electrode

In the proposed cell design, EIS on microelectrodes were measured against large, porous silver counter electrode. The counter electrode area was by design made large enough (~ 60 times the area of the working electrode) to minimize its contribution to the overall impedance at all frequencies such that impedance response of the working electrode only is observed. To quantify the effect of counter electrode on cell impedance, impedance data for two identical microelectrodes were obtained against a common counter electrode and then against each other.

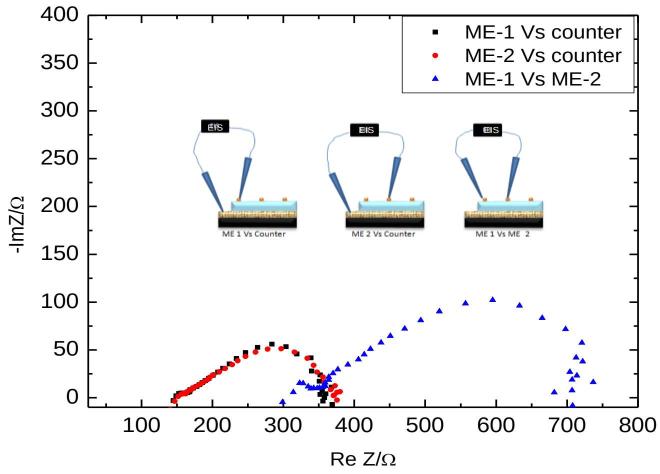

Figure 3-8 Impedance response of the cell in different configuration (■- microelectrode 1 (ME-1) Vs counter electrode ●-microelectrode 2 (ME-2) Vs counter ▲ -microelectrode 1 (ME-1) Vs Microelectrode -2(ME-2)

The results are presented in Figure 3-8. If the effect of counter electrode was negligible, then electrode polarization resistance (R_p) of each microelectrode measured against large counter electrode should be half of R_p measured against each other. From the Figure 3-8, it is evident that impedance of microelectrode 1(220Ω) and microelectrode 2 (219Ω) against counter electrode is half of the impedance measured against each other (438Ω). Therefore, it can be concluded that effect of counter electrode is negligible to overall impedance.

3.3.4 Reproducibility of electrochemical performance data

As discussed earlier, a major advantage of the micro-electrode test system is that it allows measurement on multiple electrodes in a short period of time without the need to load/unload electrodes and heat/cool the test system. Further, collection of data on multiple electrodes permits the assessment of electrode performance reproducibility on a statistically significant sample. Figure 3-9 (a) shows impedance spectra of nine identically fabricated microelectrodes. The Ohmic resistance and polarization resistance for the microelectrodes are reported in Fig 3.10 and Table 3-2. Variation in impedance spectra of each identical electrochemical cell may be due to variability in the electrode geometry.

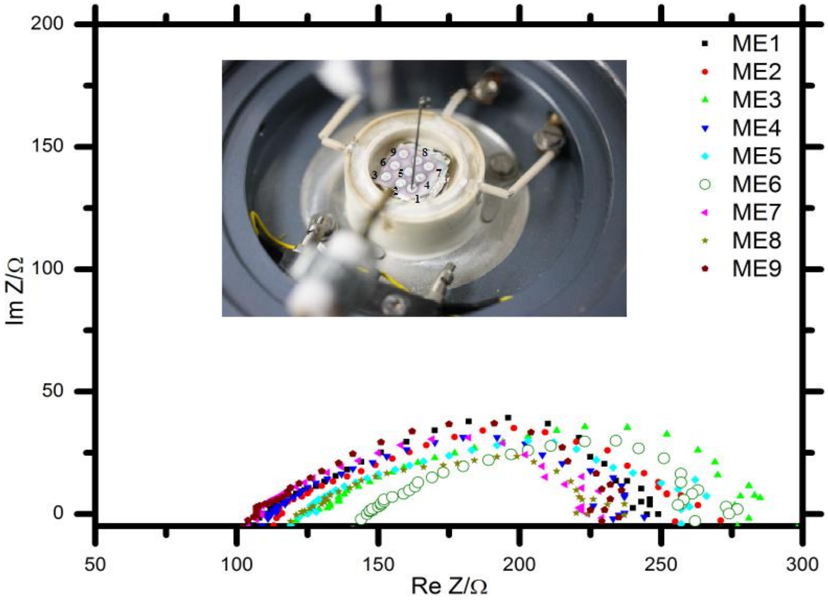

Figure 3-9 Impedance spectra of nine identical microelectrodes at 525 °C in air

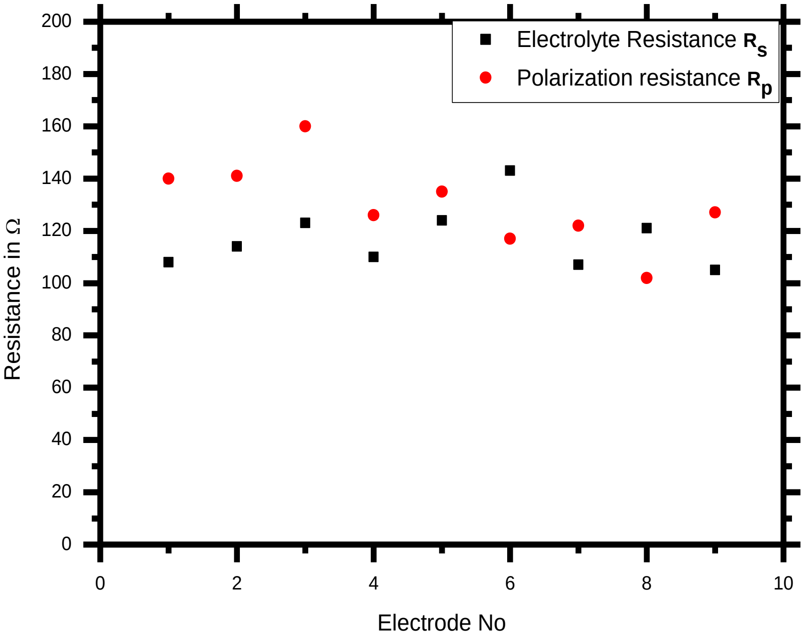

Figure 3-10 Distribution of R_p and R_s of identical microelectrodes at 525 °C in air

Data collected from nine identical cells were analyzed to obtain statistical information about the electrode performance. The results are presented in Table 3-3. For a given data set $(x_1, x_2 \ldots x_n)$with the mean $(\bar{X})$, the standard deviation (s_{n-1}) is a measure of how the given data set was spread out, which can be determined by the following expression:

$$s_{n-1} = \sqrt{\left(\frac{1}{n-1}\sum_{i=1}^{n}(x_i - \bar{X})^2\right)} \qquad 3\text{-}1$$

Table 3-3 Statistical Analysis of Ohmic resistance and electrode polarization resistance for nine identical electrodes

Temperature (°C)	**Ohmic Resistance (Ohm)**		**Electrode Polarization (Ohm)**	
	Mean	Standard Deviation	Mean	Standard Deviation
460	325	45	738	110
500	159	20	208	31
525	117	12	130	17

3.3.5 Analysis of Ohmic resistance

The Ohmic resistance may arise from electrolyte resistance associated with oxide ion transport through the YSZ single crystal electrolyte and inherent resistance of measuring system such as conduction of electrons in the probe needle, wire, and circuits (i.eOhmic resistance = electrolyte resistance + resistance due to lead wires). Therefore, resistance due to the lead wires was determined as 10 Ohms by short circuiting two probes and subtracted from Ohmic resistance in order to deduce the electrolyte resistance.

The electrolyte resistance can be related to intrinsic ionic conductivity of electrolyte and geometric factor that determine the ionic path of my system:

$$\sigma_{ionic} = \frac{\text{Electrolyte Thickness}}{R_s \times \text{ Area}} \qquad 3\text{-}3$$

In our case, electrolyte thickness was 0.5 mm and area of the working electrode was considered as 3.1 mm^3

The activation energy for oxygen ion conductivity in YSZ electrolyte can be determined using following expression

$$\sigma_{ion} = \frac{A}{T} exp^{\frac{-E_a}{kT}} \qquad 3\text{-}4$$

where, k is Boltzmann constant, A is pre exponential factor and E_a is activation energy. The ionic conductivity determined at three different temperatures by applying equation 3-3 were plotted on an Arrhenius type plot (lnσ Vs 1/kT) as shown in Figure 3-11. The activation energy was determined as 0.93 eV, which is in very good agreements with literature data for oxygen ion conduction in YSZ [16-17].

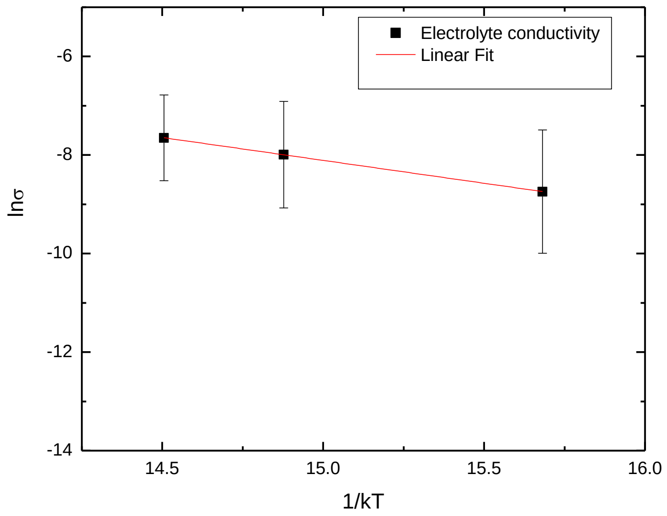

Figure 3-11 Arrhenius plot of electrolyte conductivity

3.3.6 Analysis of electrode polarization resistance

3.3.6.1 Electrode Processes

As depicted in Figure 3-12, ORR processes at cathode /electrolyte interface involves multistep processes. The major processes during oxygen reduction may include adsorption of oxygen on to cathode surface, dissociation of adsorbed oxygen molecule into oxide ion, surface diffusion of oxygen molecule/oxide ion from cathode surface to triple phase boundary, incorporation of oxide ion into cathode bulk, incorporation of oxide ion at the triple phase boundary into electrolyte bulk, diffusion of oxide ion through cathode bulk, interfacial charge transfer and oxide ion transport through electrolyte.

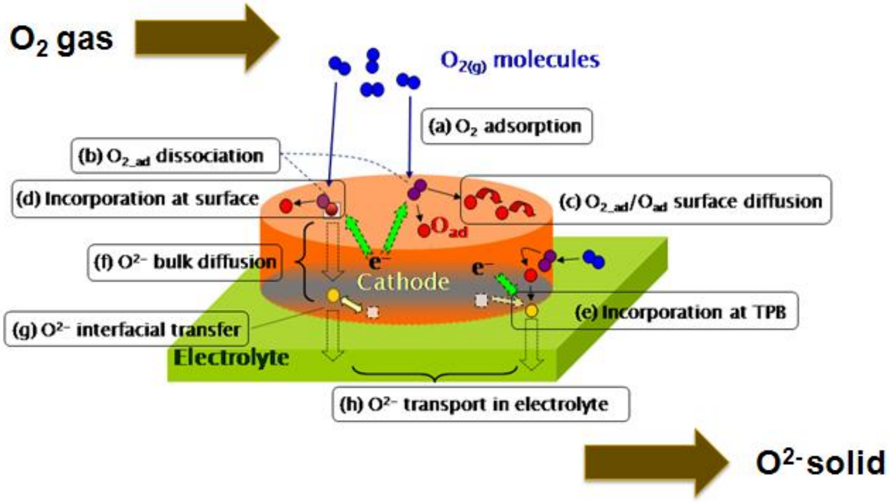

Figure 3-12 Possible reaction mechanisms of oxygen reduction reactions (ORR) on SOFC cathodes (reproduced from [39])

3.3.6.2 Fitting of Impedance Data

The impedance spectra for Ag/YSZ/Ag system, shown in Figure 3-13, exhibits two semicircles indicating that at least two different processes occurs with distinct time scales. From the discussion in the preceding section it may be appreciated that the deconvolution of the impedance spectra and the identification of rate-limiting step is difficult [28-33].Fortunately, the ORR behavior at Ag/electrolyte interface has been well studied and reported by others [34-38]. This is one of the reasons for choosing Ag/YSZ system to validate my test setup rather than examining complex perovskite/YSZ interface. It has been proposed that the high-frequency (HF) semicircle may originate from charge-transfer reaction at the electrode–electrolyte interface, and the low-frequency (LF) semicircle is a consequence of a slow process such as diffusion of oxide ion through silver bulk [34-35]. Recently, Sasaki *etal* studied ORR kinetics at Ag/electrolyte interface using secondary-ion mass spectroscopy (SIMS) and confirmed similar mechanism that the overall reduction process is limited by oxide ion diffusion through Ag bulk and its interfacial charge transfer process [37-38].

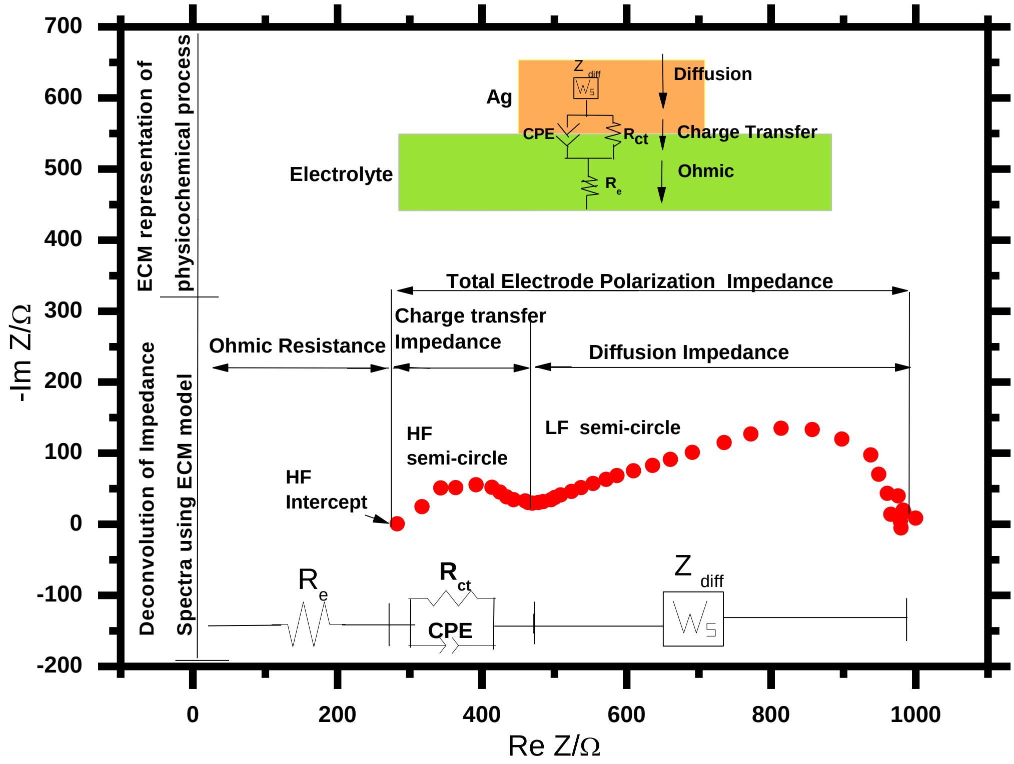

Figure 3-13 Schematic representation of physiochemical process, impedance spectra and electrical circuit model (ECM) at Ag/YSZ interface.

An equivalent electrical circuit model (ECM), commonly employed for many other electrode processes, as shown in Figure 3-13 was used to fit the impedance response. A complex nonlinear least-square method (CNLS) was used to identify the structure and/or parameters of the ECM. Z-view software (Scribner Associates Inc, Southern Pines, US) developed for the implementation of CNLS was adopted for model fitting.

3.3.6.2 Analysis of high-frequency and low-frequency responses of the impedance spectra

The high-frequency impedance response is commonly attributed to the charge-transfer process at interface. The impedance of charge-transfer process (Z_{ct}) is represented by resistance –capacitance parallel circuit.

$$Z_{ct}=\frac{1}{\frac{1}{R_{ct}}+i\omega C_{dl}} \qquad 3\text{-}5$$

R_{ct} represent charge transfer resistance and C_{dl} represent double layer capacitance at interface. Usually, constant phase element (CPE) is used in the place of capacitive impedance to take into account the “non-ideality” of experimentally observed semicircles [25-27]. The impedance of CPE (Z_{CPE}) is represented as

$$Z_{CPE}=\frac{1}{Q(i\omega)^{P}} \qquad 3\text{-}6$$

where, Q represents non-ideal capacitance and parameter P is a measure of the degree of “depression” of semi-circle arc. For P = 1, the constant phase element is identical to a capacitance, corresponding to a perfect semicircle.

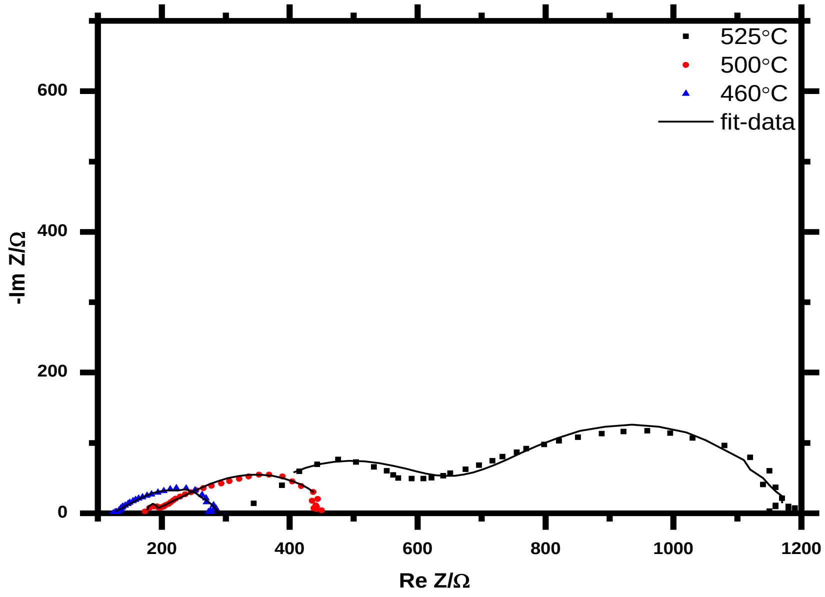

Figure 3-14 Typical impedance spectra of Ag/YSZ/Ag system at 3 different temperatures. Lines are fit of ECM (of Fig 3-13) to the data.

The low-frequency response is attributed to diffusion impedance of oxide ion inside silver bulk. An ideal diffusion process of impedance spectra can be represented as Warburg element (W) in equivalent circuit model (ECM) and expressed as

$$Z_{diff} = R_{diff}\,\frac{\tanh\left(\left(\frac{L^2}{D}(i\omega)\right)^P\right)}{\left(\frac{L^2}{D}(i\omega)\right)^P} \qquad 3\text{-}7$$

where, R_{diff} represent diffusion resistance, L represents diffusion length and D represents oxide ion diffusion co-efficient. The parameter P is usually fixed to 0.5 but varies between 0.25 and 0.7 in a non-uniform diffusion process.

Experimental data were fitted with equivalent circuit model to obtain parameters such as R_{ct} ,R_{diff} were estimated. The results are presented in Table 3-4.

Table 3-4 Equivalent circuit model fit parameters for impedance response of nine identical electrodes. The mean values and standard deviation are reported.

Temperature	**R_{ct}**	**R_{diff}**
460	**137.4± 39.8**	**604.4 ± 96.5**
500	**9.8 ±2.3**	**204.2 ± 37.8**
525	**3.4 ± 0.9**	**133.8 ± 23.1**

In addition, activation energy (E_a) can be determined from the resistance value using the relationship

$$\frac{1}{Resistance} = K(T)\, e^{\frac{-E_a}{RT}} \qquad 3\text{-}8$$

where, E_a is activation energy and R is a gas constant.

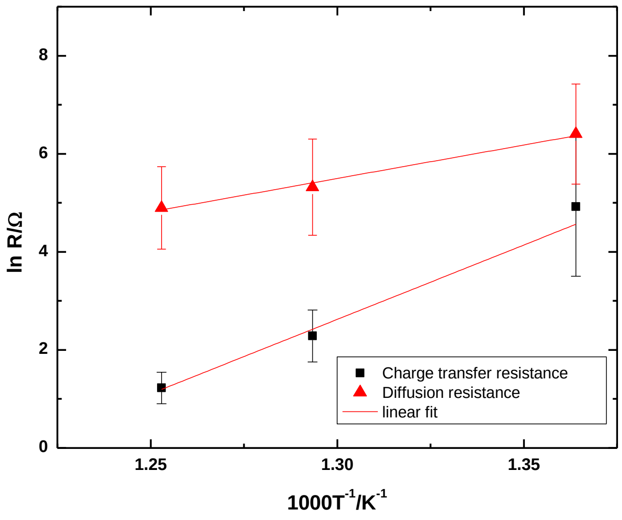

Figure 3-15 Arrhenius plot of charge transfer and diffusion resistances

From the graph, the activation energy of charge transfer resistance and diffusion resistance were determined as 2.9 eV, and 1.19 eV, respectively.

3.4 Conclusion

Miniature Ag electrodes on YSZ substrate using the drop-on-demand inkjet printing technique were successfully fabricated. For electrochemical testing of these electrodes, a micro-contact impedance system was setup and commissioned. Testing protocol for micro-contact impedance measurements was developed. The test methods were successfully applied to study oxygen reduction reaction of nine identical Ag cathodes. Results for nine electrodes allowed the quantification of electrode-to-electrode variation.

The key contributions of this work are two-fold: (i) successful demonstration of inkjet printing in fabricating multiple electrodes, of controllable features, on a single substrate, and (ii) rapid testing of multiple electrodes to generate statistically significant performance data. The developed electrode fabrication method and micro-contact impedance setup can be applied for studies of new cathode materials in the future.

3.5 Reference

1) Wachsman, E. D.; Lee, K. T. Lowering the Temperature of Solid Oxide Fuel Cells. *Science* **2011**, *334*, 935-939.
2) Wachsman, E. D.; Singhal, S. C. Solid Oxide Fuel Cell Commercialization, Research and Challenges. *American Ceramic Society Bulletin* **2010**, *89*, 22-32.
3) Potyrailo, R. A.; Rajan, K.; Stowe, K.; Takeuchi, I.; Chisholm, B.; Lam, H. Combinatorial and High-Throughput Screening of Materials Libraries: Review of State of the Art. *ACS Combinatorial Science* **2011,***6*, 579–633.
4) Baerns, M.; Holeňa, M. In *Combinatorial development of solid catalytic materials: design of high-throughput experiments, data analysis, data mining;* Imperial College Press: 2009; Vol. 7.

5) Potyrailo, R. A.; Maier, W. F. In *Combinatorial and high-throughput discovery and optimization of catalysts and materials;* CRC Taylor & Francis: Boca Raton, FL, 2007.

6) Hagemeyer, A.; Strasser, P.; Volpe, A. F. In *High-throughput screening in heterogeneous [i.e. chemical] catalysis;* Wiley-VCH: Weinheim; [Great Britain], 2004 .

7) Mohebi, M. M.; Evans, J. R. G. A Drop-on-Demand Ink-Jet Printer for Combinatorial Libraries and Functionally Graded Ceramics. *J. Comb. Chem.* **2002**, *4*, 267-274.

8) Evans, J.; Edirisinghe, M.; Coveney, P.; Eames, J. Combinatorial Searches of Inorganic Materials using the Ink-Jet Printer: Science, Philosophy and Technology. *Journal of the European Ceramic Society* **2001**, *21*, 2291-2299.

9) deGans, B. J.; Duineveld, P. C.; Schubert, U. S. Inkjet Printing of Polymers: State of the Art and Future Developments. *Adv Mater* **2004**, *16*, 203-213.

10) Tekin, E.; Smith, P. J.; Hoeppener, S.; van den Berg, A. M. J.; Susha, A. S.; Rogach, A. L.; Feldmann, J.; Schubert, U. S. Inkjet Printing of Luminescent CdTeNanocrystal–Polymer Composites. *Advanced Functional Materials* **2007**, *17*, 23-28.

11) Ago, H.; Murata, K.; Yumura, M.; Yotani, J.; Uemura, S. Ink-Jet Printing of Nanoparticle Catalyst for Site-Selective Carbon Nanotube Growth. *Appl. Phys. Lett.* **2003**, *82*, 811.

12) Tomov, R.; Krauz, M.; Jewulski, J.; Hopkins, S.; Kluczowski, J.; Glowacka, D.; Glowacki, B. Direct Ceramic Inkjet Printing of Yttria-Stabilized Zirconia Electrolyte Layers for Anode-Supported Solid Oxide Fuel Cells. *J. Power Sources* **2010**, *195*, 7160-7167.

13) Sukeshini, A.; Cummins, R.; Reitz, T.; Miller, R. Inkjet Printing of Anode Supported SOFC: Comparison of Slurry Pasted Cathode and Printed Cathode. *Electrochemical and Solid-State Letters* **2009**, *12*, B176.

14) Rossiny, J.; Fearn, S.; Kilner, J.; Zhang, Y.; Chen, L. Combinatorial Searching for Novel Mixed Conductors. *Solid State Ionics* **2006**, *177*, 1789-1794.

15) Fearn, S.; Rossiny, J.; Kilner, J.; Zhang, Y.; Chen, L. High Throughput Screening of Novel Oxide Conductors using SIMS. *Appl. Surf. Sci.* **2006**, *252*, 7159-7162.

16) Baumann, F.; Fleig, J.; Habermeier, H. U.; Maier, J. $Ba_{0.5}Sr_{0.5}Co_{0.8}Fe_{0.2}O_{3\text{-delta}}$ Thin Film Microelectrodes Investigated by Impedance Spectroscopy. *Solid State Ionics* **2006**, *177*, 3187-3191.

17) Baumann, F.; Fleig, J.; Cristiani, G.; Stuhlhofer, B.; Habermeier, H. U.; Maier, J. Quantitative Comparison of Mixed Conducting SOFC Cathode Materials by Means of Thin Film Model Electrodes. *J. Electrochem. Soc.* **2007**, *154*, B931.

18) Baumann, F. S.; Fleig, J.; Habermeier, H. U.; Maier, J. Impedance Spectroscopic Study on Well-Defined (La, Sr)(Co, Fe) $O_{3-\delta}$ Model Electrodes. *Solid State Ionics* **2006**, *177*, 1071-1081.

19) Brichzin, V.; Fleig, J.; Habermeier, H. U.; Cristiani, G.; Maier, J. The Geometry Dependence of the Polarization Resistance of Sr-Doped $LaMnO_3$ Microelectrodes on Yttria-Stabilized Zirconia. *Solid State Ionics* **2002**, *152*, 499-507.

20) Brichzin, V.; Fleig, J.; Habermeier, H. U.; Maier, J. Geometry Dependence of Cathode Polarization in Solid Oxide Fuel Cells Investigated by Defined Sr-Doped LaMnO Microelectrodes. *Electrochemical and Solid-State Letters* **2000**, *3*, 403.

21) Shao-Horn, Y. Oxygen Surface Exchange Kinetics on Sr-Substituted Lanthanum Manganite and Ferrite Thin-Film Microelectrodes. *J. Electrochem. Soc.* **2009**, *156*, B816.

22) Shao-Horn, Y. Thickness Dependence of Oxygen Reduction Reaction Kinetics on Strontium-Substituted Lanthanum Manganese Perovskite Thin-Film Microelectrodes. *Electrochemical and Solid-State Letters* **2009**, *12*, B82.

23) Soltman, D.; Subramanian, V. Inkjet-Printed Line Morphologies and Temperature Control of the Coffee Ring Effect. *Langmuir* **2008**, *24*, 2224-2231.

24) Deegan, R. D.; Bakajin, O.; Dupont, T. F.; Huber, G.; Nagel, S. R.; Witten, T. A. Contact Line Deposits in an Evaporating Drop. *Physical Review E* **2000**, *62*, 756.

25) Barsoukov, E.; Macdonald, J. R. In *Impedance spectroscopy: theory, experiment, and applications;* John Wiley and Sons: 2005.

26) Leonide, A. In *SOFC modelling and parameter identification by means of impedance spectroscopy;* KIT Scientific Publishing: 2009;

27) Orazem, M. E.; Tribollet, B. In *Electrochemical impedance spectroscopy;* Wiley-Interscience: 2008; Vol. 48.

28) Adler, S. B. Factors Governing Oxygen Reduction in Solid Oxide Fuel Cell Cathodes. *Chem. Rev.* **2004**, *104*, 4791-4844.

29) Adler, S.; Bessler, W. Elementary Kinetic Modeling of Solid Oxide Fuel Cell Electrode Reactions. *Handbook of Fuel Cells-Fundamentals, Technology and Applications.John Wiley and Sons* **2009**.

30) Fleig, J.; Maier, J. The Polarization of Mixed Conducting SOFC Cathodes: Effects of Surface Reaction Coefficient, Ionic Conductivity and Geometry. *Journal of the European Ceramic Society* **2004**, *24*, 1343-1347.

31) Schichlein, H.; Müller, A.; Voigts, M.; Krügel, A.; Ivers-Tiffée, E. Deconvolution of Electrochemical Impedance Spectra for the Identification of Electrode Reaction Mechanisms in Solid Oxide Fuel Cells. *J. Appl. Electrochem.* **2002**, *32,* 875-882.

32) Smith, J.; Chen, A.; Gostovic, D.; Hickey, D.; Kundinger, D.; Duncan, K.; DeHoff, R.; Jones, K.; Wachsman, E. Evaluation of the Relationship between Cathode Microstructure and Electrochemical Behavior for SOFCs. *Solid State Ionics* **2009**, *180*, 90-98.

33) Wachsman, E. D.; Center, U. F. D. O. E. H. T. E. Deconvolution of SOFC Cathode Polarization. *ECS Trans* **2007**, *7*, 1051.

34) Jimenez, R.; Kloidt, T.; Kleitz, M. Reaction-Zone Expansions and Mechanism of the O, Ag/Yttria-Stabilized Zirconia Electrode Reaction. *J. Electrochem. Soc.* **1997**, *144*, 582.

35) Van Herle, J.; McEvoy, A. Oxygen Diffusion through Silver Cathodes for Solid Oxide Fuel Cells. *Journal of Physics and Chemistry of Solids* **1994**, *55*, 339-347.

36) Wang, J. H.; Liu, M. L.; Lin, M. Oxygen Reduction Reactions in the SOFC Cathode of Ag/CeO_2. *Solid State Ionics* **2006**, *177*, 939-947.

37) Sasaki, K.; Muranaka, M.; Suzuki, A.; Terai, M. In *In Ag thin film cathode for LSGM electrolyte LT-SOFCs;* ECS Transactions: 2007, 7, 1311- 1318.

38) Sasaki, K.; Muranaka, M.; Suzuki, A.; Terai, T. Determination of Oxygen Pathway in Silver Cathodes by Secondary-Ion Mass Spectroscopy using Oxygen Isotope Exchange. *J. Electrochem. Soc.* **2011**, *158*, B1380.

39) Lee, Y.L. and Gadre, M. Ab Initio Studies of Solid Oxide Fuel Cell Cathode Materials*http://matmodel.engr.wisc.edu/Nuggets/Yueh-Lin_SOFC.html* (accessed 03/02, 2012).

Chapter 4

Conclusions and Recommendations

This thesis addresses two distinct problems related to the development of low-temperature SOFC cathodes. The first issue, discussed in Chapter 2, investigates the chemical stability of a new cathode material, $La_{0.5}Ba_{0.5}CoO_3$ (LBC) in carbon dioxide atmosphere. The second issue, discussed in Chapter 3, is the combined development of fabrication of electrodes of reproducible characteristics and a test system for rapid testing of multiple electrodes.

4.1 Reaction of LBC with CO_2

This thesis is the first study that examined in depth the reactivity of a potentially promising SOFC cathode material, $La_{0.5}Ba_{0.5}CoO_3$, with carbon dioxide. Through a combination of different techniques - thermogravimetric analysis, ex-situ XRD analyses of reacted products, and in-situ XRD analysis – the pathway for reaction of LBC with CO_2 was established. A significant scientific contribution arising from the study is the generation of the thermodynamic phase boundary for carbonate formation in the LBC-CO_2 system. The analysis of data yielded fundamental thermodynamic parameters - the standard state enthalpy (ΔH^o) and the standard state entropy (ΔS^o) – for the carbonation reaction. This is an original scientific contribution. A direct application of the completed thermodynamic study of the LBC-CO_2 reaction system was in the prediction of the safe operating conditions for LBC-based cathode fed by ambient air that contains ~380 ppm CO_2.

4.1.1 Recommendations for future work

In this study the effect of carbon dioxide on structural and chemical change of LBC was studied over operating temperature range pertinent to SOFC application. It is recommended that impact of carbonation on electrocatalytic properties under actual operating conditions, i.e. under electrical polarized conditions, should be studied.

Secondly, fundamentally a heterogeneous reaction like carbonate formation in a LBC-CO_2 system is a multiple-step process. Further knowledge of each step and understanding their kinetics would be vital for designing material with improved performance and develop mitigation strategies.

4.2 Development of test system for rapid testing of multiple electrodes

The original goal of developing a test system for rapid testing of multiple electrodes such that statistically significant performance data could be generated was accomplished. An associated goal of fabricating electrodes with reproducible features was also accomplished. The feasibility of fabricating multiple electrodes, of reproducible features, on a single substrate and rapid testing of the multiple electrodes was successfully demonstrated via the testing of an electrochemical cell system with nine identical working electrodes and a common counter electrode. The significance of the contribution of this work is that the test protocols developed for fabrication and testing of multiple miniature electrodes on a single substrate can be applied for testing of new cathode materials.

The micro-contact impedance spectroscopy (MCIS) study of Ag/YSZ of nine identical electrodes allowed the quantification of the electrode-to-electrode variation. This work is among the handful of SOFC electrode studies wherein statistically significant variability in electrode performance has been reported. In addition, equivalent circuit model (ECM) was proposed for oxygen reduction kinetics (ORR) at Ag/YSZ interface to deconvolute EIS. The proposed ECM then fitted with measured EIS to extract kinetic parameters and the estimated kinetic parameters compares well with the literature.

4.2.1 Recommendations for future work

An obvious recommendation is to apply the developed methods for fabrication and electrochemical testing of electrodes made of new cathode materials. Another recommendation is to improve the test design by incorporating a reference electrode to accommodate 3-electrode dc measurement.

Finally, current MCIS setup allows experimentation in ambient air condition. Therefore, MCIS setup should be upgraded for controlling the chemical environment such that partial pressure dependence of electrode can be studied.

Appendix A

LBC-CO_2 reaction Homogenous Model

As schematically shown in Figure A-1, a homogenous model is proposed for the LBC-Carbon dioxide reaction kinetics. Consider the reaction

$$2La_{0.5}Ba_{0.5}CoO_{3-\delta}(s) + CO_2(g) \rightarrow \ BaCO_3(s) + \ other\, phases(s) + xO_2(g) \uparrow \quad \text{A-1}$$

A simple rate expression assuming first order with respect to CO_2 and second order with respect to LBC was given as ,

$$-\frac{dC_{LBC}}{dt} = k\, C_{LBC}^2 P_{CO_2} \qquad \text{A-2}$$

where, k is rate constant , C_{LBC} is the LBC concentration and P_{CO2} is carbon dioxide partial pressure

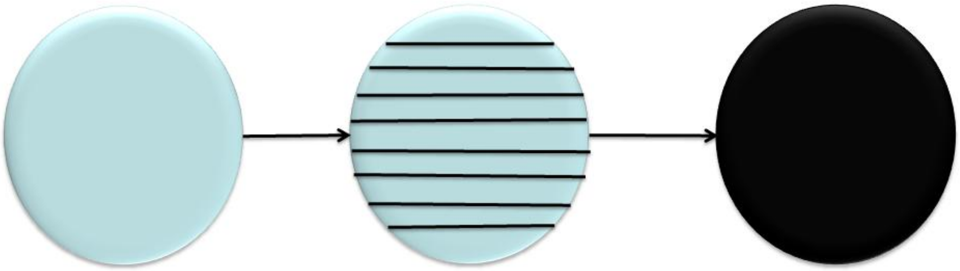

Figure A-1 Homogenous model

The reaction consider following assumption,

- The reaction is considered as homogenous in nature and effect due to surface, transport and other processes are considered negligible.
- The diffusion of gas is fast and has negligible effect on overall kinetics.

- Particle size remains constant during the reaction.
- Structural changes of LBC during reaction have negligible effect on overall kinetics.

On integration eqn 3-14 gives

$$\frac{C_{(LBC)_t}}{C_{LBC_{initial}}} = \frac{1}{1 + k \times C_{LBC_{initial}} \times P_{CO_2} \times t} \tag{A-3}$$

Reaction conversion (X_A) can be written in the form

$$X_A = 1 - \frac{C_{(LBC)_t}}{C_{LBC_{initial}}} = 1 - \frac{1}{1 + k \times C_{LBC_{initial}} \times P_{CO_2} \times t} \tag{A-4}$$

On the other hand, reaction conversion (X_A) using TGA experimental data can be defined as

$$X_A = \frac{\Delta W_t}{\Delta W_f} \tag{A-5}$$

where, ΔW_f is the final weight change and ΔW_t is weight change at time t. The model eqn A-4 and TGA experimental data is related as

$$X_A = \frac{\Delta W_t}{\Delta W_f} = 1 - \frac{1}{1 + K \times t} \tag{A-6}$$

where $K = k \times P_{CO2} \times C_{LBCinitial}$

Non linear least square analysis is applied to TGA data to determine the rate law kinetic parameter (K). Initial guesses are made to the kinetic parameter in the above model, by which conversion was computed. Excel Solver is used to minimize the sum of the squared difference of measured TGA conversion (Xm) and the computed conversion (Xc).